Summer 8-2019

The Role of Boundary-Parallel Vertical Wind Shear in Convection Initiation

Alexander J. Krull
University of Nebraska-Lincoln, akrull@huskers.unl.edu

THE ROLE OF BOUNDARY-PARALLEL VERTICAL WIND SHEAR IN CONVECTION INITATION

by

Alexander J. Krull

A THESIS

Presented to the Faculty of

The Graduate College at the University of Nebraska

In Partial Fulfillment of Requirements

For the Degree of Master of Science

Major: Earth and Atmospheric Sciences

Under the Supervision of Professor Adam L. Houston

Lincoln, Nebraska

August, 2019

THE ROLE OF BOUNDARY-PARALLEL VERTICAL WIND SHEAR IN CONVECTION INITIATION

Alexander J. Krull, M.S.

University of Nebraska, 2019

Advisor: Adam L. Houston

Convection initiation (CI) remains a forecasting challenge for meteorologists. CI frequently occurs within the vicinity of some airmass boundary or density current. Airmass boundaries are favored areas of convergence, thus associated forced ascent facilitates CI. Features such as misocyclones often develop along the leading edge of airmass boundaries, favoring updraft formation and prompting alterations to the horizontal and vertical flow near the boundary. Airmass boundary characteristics and CI potential have been found to be sensitive to the environmental vertical wind shear. This affects propagation speed, convergence, and thus forced ascent along the leading edge. Previous studies have focused primarily on the boundary-normal component of the vertical wind shear vector, assessing changes in density current depth, propagation speed, and convergence. This experiment seeks to discover how airmass boundary characteristics and CI potential are impacted by changes to the boundary-parallel component to the vertical wind shear vector. Through idealized high-resolution simulations, this study finds there is sensitivity to changes in the boundary-parallel vertical wind shear vector that affects CI potential, due to alterations in propagation speed and vertical ascent. This sensitivity is dependent on the initial temperature perturbation of the density current. The results of these simulations and an explanation of the physical processes attributed to changes in the boundary-parallel vertical wind shear are discussed.

Acknowledgements

I would like to thank my advisor, Dr. Adam Houston for the opportunity to join the Severe Storms Research Group at the University of Nebraska-Lincoln to conduct research in the field of atmospheric sciences. Thank you to my committee members, Dr. Clinton Rowe and Dr. Matthew Van Den Broeke, for their guidance along the way during this project. Thank you to Dr. Jason Keeler, for assistance with setting up Cloud Model 1 and discussion to troubleshoot early issues encountered in this project. Thank you to Dr. Luke Madaus, for excellent discussion regarding the use of CM1. Thank you Dr. Russ Schumacher for sharing code edits to CM1 to run our simulations. I would also like to thank all attendees of AMS and NWA conferences who I have engaged in discussion with regarding this work that ultimately led to new approaches and viewpoints when analyzing the results.

Thank you to Lawrence Wolfgang Hanft, Adrianne Engel, Alexander Carne, and Alexandra Caruthers for excellent scientific discussions during the course of this project. I would also like to thank members of the UNL Severe Storms Research Group and all other UNL EAS students for their helpful discussions. Thank you to the staff at the National Weather Service Des Moines, IA for their support as I finished my Master's Degree. Finally, thank you to all my family and friends for their continued support and encouragement throughout the completion of this work.

This work was made possible by CLOUD-MAP, funded by NSF EPSCoR OIA-1539070. Computing resources were provided by the University of Nebraska-Lincoln Holland Computing Center.

Table of Contents

List of Figures

List of Tables

1. Introduction

Convection initiation (CI) remains a forecasting challenge for meteorologists. Skill in predicting CI has increased with techniques such as the "ingredients approach" (Doswell 1986), as well as the development of high resolution convective allowing models (CAMs; Bryan et al. 2003). Despite these advances, CI forecasts are often far from perfect due to the limited understanding of small scale dynamics and microphysics (Roebber et al. 2004).

Thunderstorms, such as tornadic supercells, have a high-impact potential on life and property, and, therefore, CI is a topic of interest to applied research. Both observational and modeling studies have been and are currently being conducted to probe these processes to gain further insight, working toward the goal of understanding CI well enough to predict its location and timing. One such example is the International H2O Project (IHOP) of 2002 (Weckwerth and Parsons 2006). IHOP was a field campaign in the southern Great Plains that focused on airmass boundaries and associated CI. This effort has provided a rich dataset of in-situ and remotely sensed observations around boundaries that resulted in CI occurrence and CI failure. The following subsections will provide an overview of topics important to boundary evolution and CI, including research that utilized data from IHOP.

a. Features Along the Leading Edge of Boundaries

Wave-pattern structure and misocyclone development along the leading edges of density currents have been features of interest in studies regarding CI occurrence or CI failure (Weckwerth and Parsons 2006). For example, the associative relationship between CI and misocyclones is thought to be a consequence of the similarity in mechanisms

responsible for their occurrence (Crook et al. 1991; Wilson et al. 1992). However, the presence of a feature such as a misocyclone alone is not a sufficient condition for CI. Regardless of CI occurrence or failure, updrafts may still be associated with the development of wave-structure and misocyclones along the leading edge of a boundary (Lee and Wilhelmson 1997a, 1997b) and, therefore, a locally favored location for CI compared to elsewhere along the boundary.

Although wave-structures and misocyclones typically result in downward vertical pressure gradient forces (Murphey et al. 2006; Marquis et al. 2007), the asymmetric flow field around them can generate low-level convergence (Murphey et al. 2006 and Buban et al. 2012). This convergence can produce upward vertical motion by altering the fluid extension component of the vertical pressure gradient force. This favors the development of updrafts in the vicinity of these leading edge features.

With respect to CI, the control these features have in updraft distribution along a boundary is important as the forced ascent generated may largely determine if and where parcels are lifted to the level of free convection (LFC) in a particular environment (Arnott et al. 2006). The localized enhancements in the convergence and vertical velocity are attributed to the wave structure developing discontinuities within the low-level convergence and flow field along the leading edge (Buban and Ziegler 2016a, 2016b).

Although our study does not address specific wave structures or misocyclones, these previous studies have highlighted the importance of forced ascent along an airmass boundary for CI. Therefore, our study also focuses on processes that control ascent.

b. Entrainment and Lapse Rates

The most basic conceptual models of thunderstorm development are based on a parcel that rises adiabatically. However, entrainment impacts are often excluded due to its complexity and difficulty to parameterize accurately (Neggers et al. 2002). There has been success in predicting thermodynamic variables associated with entrainment in strong updrafts (Neggers et al. 2002). An inverse relationship between vertical velocity (w) and entrainment rate has also been noted. Thus, it implies entrainment has greater impacts to slower moving parcels, while faster moving parcels are less impacted by entrainment as in-cloud properties are closer to being adiabatic. This relationship between w and entrainment underpins criticality, and has been tested in cloud-resolving numerical simulations of CI (Houston and Niyogi 2007).

However, this was partially refuted in more recent work. Dilution attributable to entrainment was further characterized by determining if the initial state of the parcel, "nature", or the entrainment effects, nurture, was more impactful on a parcel's buoyancy (Romps and Kuang 2010). The correlation of mixing ratio, potential temperature (θ), and vertical velocity was low when compared to cloud-base values, and higher when compared to that of air entrained from the environment (Romps and Kuang 2010). This implies that "nurture" is more dominant in describing the variability of these parameters within a parcel. It refutes Neggers et al. (2002) by implying entrainment is stochastic and does not scale inversely with vertical velocity. Thus, understanding the ambient environment, and consideration of stochastic entrainment, are both necessary to determine the fate of the parcel and its ability to initiate deep convection.

Dawe and Austin (2012) continued to explore the topic of nature vs. nurture. Their simulations examined whole clouds, not just individual parcels. Their simulations yielded similar results; the correlation of mixing ratio and θ was weak when compared to the cloud base values and strong compared to that based on entrainment from the environment. This was particularly true at levels 1000 m above cloud base. Thus, stochastic entrainment plays a bigger role in the variation observed in clouds and parcels.

For assessing CI, the buoyancy of a parcel is a characteristic that can be used to determine the potential of parcels to reach the LFC in a given environment. Entrainment and detrainment processes describe the dilution of the parcels as they ascend. In exploring the buoyancy and dilution, considering the lapse rate in the active cloud bearing layer (ACBL) is necessary, and was done in CI sensitivity study by Houston and Niyogi (2007). Of the six lapse rates used in simulations, only the three largest resulted in deep convection initiation (DCI). Houston and Niyogi (2007) classified the lapse rates into two different regimes, supercritical and subcritical. Supercritical refers to a lapse rate in which a parcel gains buoyancy at a greater rate due to its ascent than loses buoyancy due to dilution from entrainment. Subcritical is when the parcel loses buoyancy at a greater rate than it gains buoyancy from ascent. These studies validate the importance of understanding nurture vs. nature, as the effects of dilution can hinder a parcel's ability to become buoyant and continue to freely ascend. Research related to entrainment and parcel dilution highlights the importance of needing to characterize and track the location of buoyant air, as it impacts parcels in real convective environments as they move away from the boundary. Thus in our study, the placement of buoyant air is analyzed and can be factored into the development for a CI potential proxy.

c. Low-level Vertical Shear and Cold Pool Depth

Location and timing differences in CI have demonstrated sensitivity to differing intensities of vertical wind shear (Droegemeier and Wilhelmson 1985). Observational studies have noted sensitivity to vertical wind shear, such as a cold front from IHOP in which the vorticity imbalance along the edge was attributed to vertical wind shear (Arnott et al. 2006). The vorticity imbalance did not favor optimal updraft erectness, and therefore the parcel ascent may not have been conducive to CI. Section A has displayed the kinematic and thermodynamic fields that provide insight to ascent that are critical to understanding CI potential. Thus, it is necessary to understand how vertical wind shear can affect ascent at the boundary and the entrainment in rising parcels.

The response of the boundary to the vertical extent and magnitude of ascent can be approximated by assuming that the outflow behaves as a density current that adheres to flow-force balance (Xu 1992). With this balanced condition in an environment with positive shear, where the east-west component of the wind (u) increases with height relative to a north-south oriented outflow boundary propagating from west to east, the density current exhibits greater depth and steeper frontal slope. The response is a greater propagation speed. In a negative shear environment, where u decreases with height relative to the same boundary, the density current is shallower and the slope is not as steep. The response is a slower propagation speed. An important implication for CI of a deep, fast-propagating density current with a greater frontal slope is an increase in convergence and associated increase in pressure, subsequently enhancing vertical ascent. This theoretical response is consistent with two-dimensional simulations with boundary-normal wind shear (Xu et al. 1996). Thus, w scales to the magnitude of the vertical wind

shear (Houston 2016). It is important to consider density current characteristics when assessing the role of vertical wind shear in CI occurrence or failure.

Simulations specifically focused on CI associated with density currents have also noted that convergence is sensitive to the vertical shear (Moncrieff and Liu 1999). Dependent on the regime, which considers boundary propagation direction and the surface wind vector in addition to the vertical wind shear, the density current responds with a change in head depth and convergence along the leading edge. CI potential is greater in the simulations with stronger forced ascent, as parcels receive more momentum to reach the LFC (Moncrieff and Liu 1999). The impacts to CI potential are proven to be related to changes in boundary characteristics prompted by differing vertical wind shear environments. This enhanced ascent and increased density current depth is also noted in the density current's "nose" height in Lee and Wilhelmson (1997a). In our simulations assessing the role of boundary-parallel vertical wind shear, these findings guide our focus to analyze passive-fluid tracers to track ascent and compare density current depth to other characteristics. For a given environment, this ultimately determines if there is sensitivity to altering the boundary-parallel component of the vertical wind shear vector.

d. Current CI Study

Our study explores the impacts of the boundary-parallel low-level vertical wind shear on density current characteristics and its implications for CI. The preceding literature reviewed has acknowledged the presence of the parallel component, but has primarily focused its in-depth analysis on the normal component of vertical wind shear in altering convergence, vertical ascent, and the development of features such as wave-like structures and misocyclones along the leading edge. This leaves us with an open

question, regarding whether the effects of the boundary-parallel component of the vertical wind shear are negligible, and implications for CI potential when alterations are made to it. Environments with strong shear in the vertical have been noted to promote momentum mixing (Wu and Yanai 1993), as well as scalar mixing and Kelvin-Helmholtz (KH) billow development (Mellado et al. 2013). Thus, one implication of changing the boundary-parallel vertical wind shear theoretically could be to alter this mixing and transport, and affect the development of KH-billows. If this occurs, alterations in the boundary-parallel vertical wind shear would have non-negligible effects on CI. We hypothesize that altering the boundary-parallel vertical wind shear will alter density current characteristics such as propagation speed and ascent along the leading edge through the transport of warmer air into head and development of KH-billows. Ultimately, the impacts to ascent will also impact CI potential. Analysis in this study focuses on propagation speed, vertical velocity, and passive-fluid tracer ascent to find if there is a sensitivity of density current characteristics and CI potential to the boundary-parallel vertical wind shear.

2. Data and Methodology

a. Numerical Model Configuration

This study utilizes Cloud Model 1 release 18 version 3 (CM1r18v3), a non-hydrostatic, non-linear, time-dependent, numerical model for idealized simulations of atmospheric phenomena (Bryan and Fritsch 2002). CM1 is capable of performing high-resolution simulations that adequately resolve storm-scale features. The work of Madaus and Hakim (2016) is one example that demonstrates the strength of CM1 to adequately resolve important small-scale features and processes that govern CI.

Our simulations use a horizontal grid spacing of 100 m, adequate for resolving characteristics and salient features of density currents. In the lowest 2 km, a vertical grid spacing of 50 m is used. From 2 km to 6 km, the vertical grid spacing is stretched, increasing from 50 m to 450 m. Above 6 km, the vertical grid spacing is 450 m up to the model domain top at 15 km. The grid spacing selection is similar to the works of Bryan et al. (2003), Houston and Niyogi (2007), Rousseau-Rizzi et al. (2016), and Buban and Ziegler (2016a) who examined features and characteristics similar to those examined in this study.

Two sets of simulations are conducted, a two-dimensional (X-Z) set and three-dimensional set. The primary focus of this study is on the results from the two-dimensional simulations. While the third spatial dimension adds realism, it allows for complex processes which increase the difficulty of isolating the role of boundary-parallel vertical shear in regulating processes germane to CI potential. The development of vortices along the leading edge is an example of complexity added by three-dimensionality. The absence of complex processes in two-dimensional simulations

facilitates in attributing changes to boundary characteristics and CI potential to the boundary-parallel vertical wind shear. Three-dimensional simulations will be analyzed more thoroughly in a subsequent study.

The domain size is 49.6 km in the horizontal and 15.0 km in depth. In order to have a boundary-parallel component to the vertical wind shear vector, the model domain is 3.2 km in the y-direction. However, no perturbations are placed within boundary to break the symmetry. Thus, with a slab symmetric boundary, these are effectively 2D simulations. This domain allows for 3 to 4 hours of boundary development. The western and eastern domain boundary conditions are set to open-radiative. For the boundary initialization selection, discussed further in a subsequent section, open-radiative was the only allowable option by CM1r18v3. The northern and southern boundary conditions are periodic. The surface boundary condition is set to free-slip to focus on quantifying impacts of changing low-level vertical shear without introducing uncertainty due to friction. The domain top boundary condition is also free-slip. Rayleigh damping is applied upward from 10 km AGL to control gravity waves.

This study does not include moisture in the simulations (imoist = 0, therefore all other parameters related to moisture and moisture conservation are ignored by CM1r18v3). While moisture is a critical ingredient in real atmosphere CI, the complexities that would have to be addressed are beyond the scope of this study. The exclusion of moisture does not negatively impact assessing CI potential through vertical velocity and passive-fluid tracer transport. Coriolis is active in these simulations, and is applied to the momentum perturbations.

Passive fluid tracers are turned on in the simulations. The tracers are placed in the lowest 750 m of the model domain similar to Schumacher (2015), where the tracers in this near surface layer are ingested into updrafts and their concentration analyzed at upper-levels. Tracers in the lowest 750 m of the model domain represent what would be warm-moist, conditionally unstable boundary layer air that would be present in a real convective environment. The tracers provide insight on the amount of near surface layer air that is lifted and from where it is lifted. A summary of all CM1 parameters appears in Table 2.1.

Table 2.1: Listing of the name-list parameters that were selected for the simulations conducted in this study, with brief justification for their selection.

Parameter	Option Selected	Reason/Justification
Time Step	1.0 s	Satisfies CFL criteria for grid spacing
Adaptive Time Step	Off	Simulations remain numerically stable, no need for changes.
Order of Horizontal Advection Scheme for Scalars	5	This scheme is for implicit diffusion. No CM1 parameters selected or features being examined necessitate an artificial diffusion scheme.
Order of Vertical Advection Scheme for Scalars	5	‘’
Order of Horizontal Advection Scheme for Velocities	5	‘’
Order of Vertical Advection Scheme for Velocities	5	‘’
Adjust average pressure perturbation to ensure conservation of dry-air mass	1	Ensures conservation of mass as boundary propagates across domain. Consequences likely small with less than 12 hour simulations.
Advect Scalars with WENO Scheme (Does Not Include Pressure)	Yes, On Final Runge_Kutta Step	Ensures smoothness in simulation after addition of random perturbations in cold pool.
Advect Velocities with WENO Scheme	“	“
Include Artificial Diffusion	No	No CM1 parameters selected or features being examined necessitate an artificial diffusion scheme.
Order of Diffusion Scheme	6	6th order diffusion is recommended, as 2nd order diffusion was designed for certain idealized cases that were not related to this study.

Initialization Option	2 (Dam Break Style)	[See section C]
Include Moisture	No	[See section A]
Subgrid Turbulence Scheme	TKE	100 m grid spacing is at large end for an LES, explicit turbulence likely not to provide the best representation
Calculation of Turbulence Coefficients in Turbulence Scheme	Horizontal is different from vertical	In the lowest 2 km of the domain, dx and dy are greater than dz
Lower/Upper Boundary Condition for Vertical Diffusion of all Scalers	Zero Flux	
Run Model in Direct Numerical Simulation Mode	No	Designed for specific experiments, no use for this study
Use Rayleigh Damping Near Lateral Boundaries	No	This would disrupt the the current via the cold-dam break initialization
Pressure Solver	Klemp-Wilhelmson Time-Splitting	This is the best option for simulations where dz is smaller than dx and dy
Number of Small (Acoustic) Time Steps	8	Must be an even number. This number is appropriate to maintain stability over the domain with 100 m grid spacing.
Include Coriolis Acceleration	Yes	Appropriate to have for simulations that will run for three hours
Apply Coriolis to Perturbation Winds Only	Yes	The base-state wind profile is the important variable being changed between simulations. It would be inappropriate to have Coriolis to act on this.
Include Dissipative Heating	No	If turned on, this could produce unrealistic effects in the cold pool
Include Energy Fallout Term	No	If turned on, this could produce unrealistic effects in the cold pool
Initial Topography Specification	No Terrain	Terrain is not the focus of this study
Specified Balance Assumption for Initial 3D Pressure Field	Hydrostatic Balance	This will ensure realistic boundary development and prevent spurious vertical velocity signals
Run Axisymmetric Version of Model	No	This feature is not compatible with selected domain boundary conditions
Diffusion coefficient for difforder of 6	0.04	Value keeps our simulations stable
Coriolis Parameter	9×10^{-5}	Representative of midlatitudes
Coefficient for divergence damper	0.1	Recommended value by CM1 creator
Off-centering Coefficient for Vertically Implicit Acoustic Solver	0.60	Close to be centered-in-time with a slight bias. Recommended stable value by creator
Inverse E-folding Time for Upper-level Rayleigh Damping Layer	3.333×10^{-3}	Recommended stable value by creator

Include Surface Model Fluxes	No	This would not allow for isolation of different vertical shear environments
Surface Model	No	There is no need for surface model with no surface fluxes and a free-slip lower boundary condition

b. Environment and Boundary Characteristics

Inter-experiment changes to the boundary-parallel wind shear are made through the CM1 input sounding. In this study, the airmass boundary is oriented north-south and thus $d\bar{v}/dz$ represents the boundary-parallel component of the vertical wind shear. Five values of $d\bar{v}/dz$ comprise the experiment set: 0.000 s^{-1}, 0.003 s^{-1}, 0.006 s^{-1}, 0.009 s^{-1}, and 0.012 s^{-1}. The boundary-normal wind shear ($d\bar{u}/dz$) is 0.006 s^{-1} in all vertical wind profiles (Figure 2.1).

The input sounding temperature profile is characterized by a constant lapse rate of -8.8 K km^{-1} through the troposphere. This environmental lapse rate ensures static stability and no capping inversions in these dry simulations.

For each of the five shear profiles, seven differing cold pool initial temperatures are tested. The smallest initial potential temperature perturbation (θ') is -4.0 K and the largest -10.0 K. The use of θ' in the remainder of this paper will refer to the potential temperature difference magnitude of the cold block at the model initialization. Previous work has noted that warmer boundaries were often shorn apart in high vertically sheared environments (Lee and Wilhelmson 1997). This implies that the impact of shear may not be independent of the airmass boundary temperature. Thus, differing cold pool strengths are considered to determine if sensitivity to $d\bar{v}/dz$ is also sensitive to the initial cold pool temperature. In the remainder of this paper, simulations with an initial cold block θ' of

4.0 K or 5.0 K will make up the small θ' group. Simulations $\theta' \geq 7.0$ K will make up the large θ' group.

Individual simulations will be identified with the following nomenclature: xd-yy-zzz. The x will either be 2 or 3, indicating a two-dimensional or three-dimensional simulation. The yy will be the initial absolute value of the θ', numbered 04 through 10. The zzz will represent the boundary-parallel shear environment. For example, 2d-05-003 is the two dimensional simulation with an initial density current θ' of -5.0 K and boundary-parallel vertical shear of 0.003 s^{-1}.

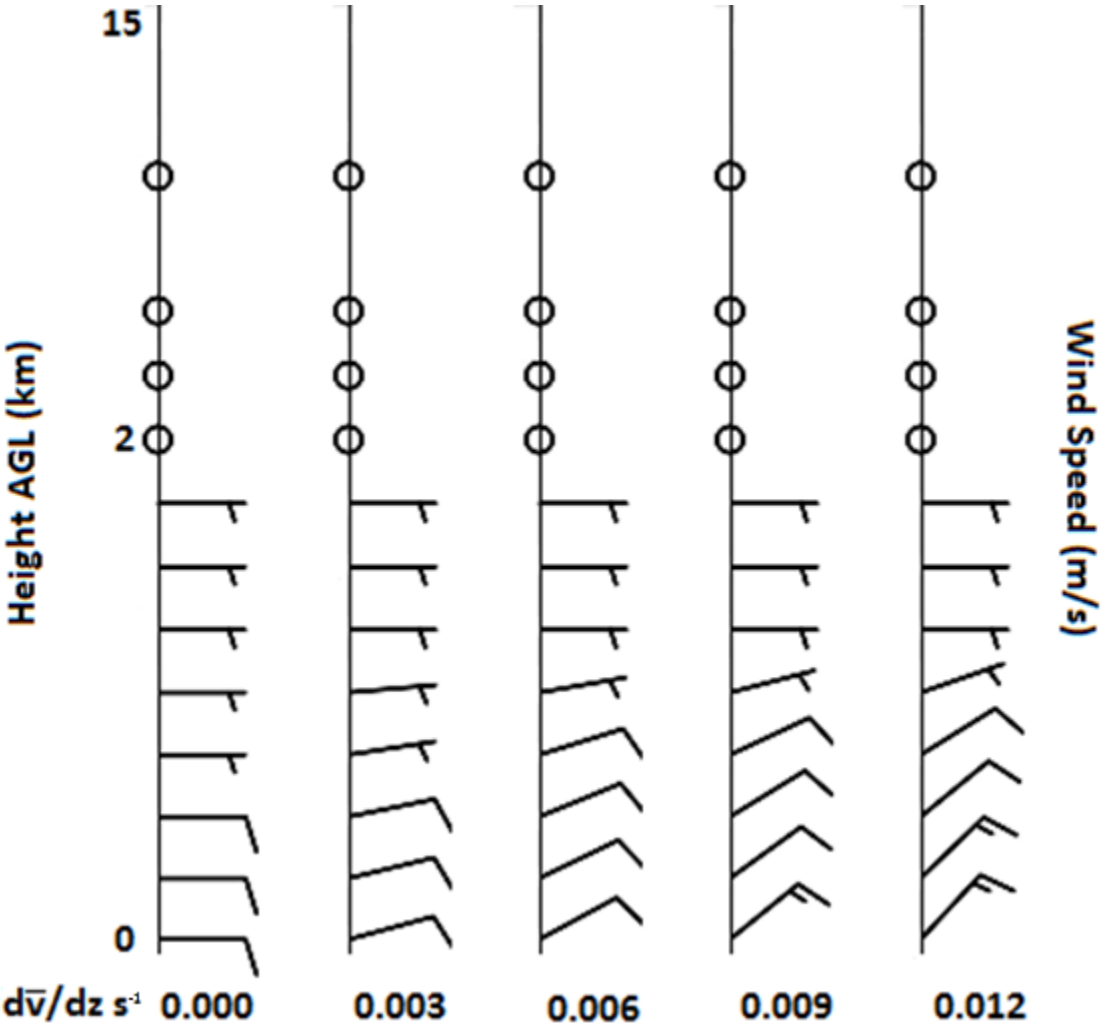

Figure 2.1: Ambient environment vertical wind profiles utilized in the simulations. The wind barbs are the total wind. Each profile represents a different boundary-parallel vertical wind shear value.

c. Airmass Boundary Initialization

To begin the simulation, CM1 is executed to initialize the airmass boundary via the cold dam break method. This option allows us the opportunity to control the initial characteristics of the outflow boundary such as initial θ' and the winds within the boundary. The leading edge of the airmass boundary is positioned 5 km east of the of the western domain edge, a distance that ensures the boundary is not forced backward off the western domain edge. Additionally, the open-radiative boundary condition will aid in maintenance of the density current by providing a source of cold air. The depth of all density currents is initially 1.5 km. The model execution is then paused at one second to zero-out the *u*-component of the wind within the density current. This is done to allow for a more natural evolution of the density current. This method was also used in Houston (2016). CM1 is then restarted with the zeroed out *u*-component winds within the density current, and run through 10800 s. A grid translation is imposed after the airmass boundary travels 30 km to keep the leading edge from exiting the domain, while preserving as much of the wake as possible.

d. Analysis Tools

The algorithm used to calculate boundary propagation speed is based on the passive fluid tracers. The simulations have passive fluid tracers in the lowest 750 m of the model domain, only on the warm side. The value used for passive fluid tracers in this region is 0.01 kg kg^{-1}. Thus, tracer values of the cold outflow air are 0.00 kg kg^{-1}. At the lowest model level, the algorithm searches all grid points in the x-direction (east to west), finding in each 60 second output time step the farthest east grid point that contains no tracers. At each output time step, the boundary propagation speed is calculated using the

current position of the farthest east no tracer location and the position five minutes prior. Calculating the propagation speed between each 60 second time step produced noisy results that were very difficult to interpret and used to assess differences between boundary-parallel shear environments, thus this box-car smoother method resolves this issue. Note that in scatter plots that display propagation speed, the points will appear to be binned at certain speeds. This is due to the algorithm's dependency on the leading edge of the boundary crossing to the next horizontal grid point. The relationship between propagation speed and the other CI proxy fields are discernable even with this bin-like appearance. Additionally, there will be a data gap in time series figures that utilize propagation speed. This occurs in simulations where grid translation had to be turned on. This is due to the box-car smoother style of the propagation speed algorithm. This is left as a gap in the data, as interpolating values during this time period may lead to misleading values and representation of the processes in the simulations.

Analysis of vertical motion is focused on the position of the leading edge near the surface. This encompasses grid points within 500 m horizontally of the leading edge at the surface and vertically to the domain top. To ensure appropriate comparisons and correlation calculations to propagation speed, the same five minute box-car smoother calculation method at each output time step is done with maximum vertical velocity. This also allowed time series plots to highlight the sequence of boundary-parallel shear environments well.

The ascent depth is used as a proxy for determining the extent of forced ascent. A value of 2.0 m s^{-1} is chosen as a minimum vertical velocity to define the depth of ascent, as slower velocity thresholds produced noisy results in depth of ascent.

Vertical velocity and ascent depth provide insight to the forcing available for air to move vertically. However, they fall short by not directly quantifying the vertical displacement of air that occurs. Passive-fluid tracers are generally used to characterize the movement of air above the density current and as a proxy for CI potential in addition to vertical velocity and ascent depth. The average tracer concentration is calculated for a boxed area that is 5 km behind and 1 km ahead of the surface leading edge position horizontally, and vertically between 1 km and 2 km AGL. The average tracer concentration value in this box, which is just above the density current head and along the leading edge, is then compared between boundary-parallel shear environments. Because the passive-fluid tracers originate in the warm inflow, the average tracer concentration within this area quantifies how much air from the warm side of the boundary is forced aloft. The average tracer concentration, expressed as a percentage, is also used to infer the amount of dilution due to entrainment (100% concentration referring to air from the lowest levels on the warm side). This can be used to make inferences regarding the residence time of parcels in areas of forced ascent, which Dawe and Austin (2012), and Houston and Niyogi (2007) demonstrate to be important factors. A higher tracer concentration means less dilution, and, ostensibly, higher buoyancy in less idealized conditions where moisture and latent heat are permitted.

Student *t*-tests are performed on the means of the differences in each CI proxy field between boundary-parallel vertical wind shear environments. The test considers a 99.99% confidence interval to determine statistical significance. Thus, differences with $|t| > 2.6$ ($p < 0.01$) are significant. The *t*-test calculations include all time points to encompass simulations in their entirety. All differences are calculated as low shear

environments minus high shear. Therefore, $t < 0$ indicates that lower shear produces a lower value (i.e. ascent depth) than the higher shear environment it is compared to, while $t > 0$ is the opposite. The sign of significant *t* results guide which time period we discuss in detail for a given set of simulations. In general, these are also the time periods that exhibit the greatest separation between shear environments. By selecting time periods that correspond to the *t*-test results, we ensure that we are assessing results that are representative of the simulations as a whole. Separation between shear environments in some of the CI proxy fields do appear in time periods that are not focused on in detail. These time periods of separation do not correspond to the sign of *t*, and thus may not be the best representation of the simulations as a whole. Further, when the time periods that we focus on are removed from the dataset, the *t*-test results are no longer significant. This means that the time periods we focus on are the largest contribution to the significant differences.

3. Results

a. Vertical Velocity, Ascent Depth, and Passive Fluid Tracer Displacement

Maximum *w* is utilized as one proxy for CI in our simulations. While differences between boundary-parallel vertical shear environments for a given θ' are not always monotonic, there are evident separation sequences that start as early as 4000 s in a few instances, and as late as 6000 s in others. Assessing maximum *w* in simulations with an initial cold block θ' = 4.0 K, 2d-04-003 and 2d-04-006 are the greatest with 6.79 and 6.99 m s^{-1}, respectively around 5340 s into the simulation (Figure 3.1a). The slower *w* occurs with 2d-04-009 and 2d-04-012 around the same time: 4.50 and 5.00 m s^{-1}, respectively (Figure 3.1a). This is a difference of just under 2.0 m s^{-1} between the fastest and slowest maximum *w*. The greatest difference, between 2d-04-006 and 2d-04-012, is characterized by a *t* of 4.56. With θ' = 4.0 K, only the differences of 2d-04-000 vs 2d-04-012 and 2d-04-003 vs 2d-04-012 are insignificant as determined by the student *t*-test (Table 3.1). The eight other comparisons between the remaining boundary-parallel vertical wind shear environments are significant, with *t* ranging between 3.31 and 14.82.

The sequence of differences in maximum *w* between boundary-parallel vertical shear environments is nearly monotonic in simulations with θ' = 5.0 K (Figure 3.1b). The fastest is 2d-05-000 with a maximum *w* of 7.31 m s^{-1} 6961 s into the simulation. The lowest values are in 2d-05-009 and 2d-05-012 with *w* of 4.00 and 4.50 m s^{-1}, respectively near the same time. This makes for a difference of ~2.5 m s^{-1} between the low and high boundary-parallel vertical wind shear environments. The differences in 2d-05-000 vs 2d-05-012 are characterized by a *t* of 12.64, and 2d-05-000 vs 2d-05-009 a *t* value of 13.39. Only 2d-05-006 vs 2d-05-009 is not significant, while the remaining nine comparisons of

boundary-parallel vertical wind shear environments are significant ranging in *t* magnitude from 7.17 to 13.39 (Table 3.1).

Analysis of boundary-parallel vertical wind shear environments with $\theta' = 4.0$ K and 5.0 K demonstrates statistically significant separation. The separation in $\theta' = 5.0$ K reveals a sequence of low boundary-parallel shear environments associated with greater maximum *w* values, and high boundary-parallel vertical shear environments with lower maximum *w* values (Table 3.1). The $\theta' = 4.0$ K simulations are not necessarily monotonic as they are in $\theta' = 5.0$ K. However, the two lowest maximum *w* in $\theta' = 4.0$ K are associated with the two highest boundary-parallel vertical wind shear environments, consistent with $\theta' = 5.0$ K simulations during their periods of greatest separation.

The differences in maximum *w* between boundary-parallel vertical wind shear environments are not distinguishable when the θ' is increased to 6.0 K (Figure 3.1c). Further, they do not demonstrate a sequence between low and high boundary-parallel vertical wind shear. However, the student *t*-test results of the differences between shear environments are significant in nine of ten possible comparisons (Table 3.1). Although statistically significant, the magnitude of *t* in the $\theta' = 6.0$ K simulations are generally "small" (less than 10.0), while significant differences in $\theta' = 4.0$ K and 5.0 K are characterized by generally large *t* magnitudes (greater than 10.0) in multiple boundary-parallel vertical wind shear environment comparisons. Thus, despite statistical significance, the small separation and lack of a notable sequence make it difficult to argue that there are robust differences in the sensitivity of maximum vertical motion to the boundary-parallel vertical shear.

When the θ' is increased to 7.0 K, separation between boundary-parallel vertical wind shear environments does appear around 7000 s and beyond (Figure 3.1d). However, the separation is not as evident as it is in θ' = 4.0 K and 5.0 K and is generally characterized by "smaller" *t* (Table 3.1). Although the sequence is not monotonic, the lowest two shear environments are associated with the two lowest maximum *w* values in the last 2000 s of the simulation. This is opposite of the lowest two boundary-parallel vertical wind shear environments in the θ' = 5.0 K simulations. Eight of the ten shear comparisons are statistically significant, with *t* magnitudes ranging from 3.07 to 6.29 (Table 3.1). As in θ' = 6.0 K, all *t* statistics are less than 10.0 in magnitude. Of the eight significant differences between shear environments, six of the *t* statistics are negative, indicating that the higher shear environments are associated with greater maximum *w*. This is also opposite of the θ' = 5.0 K simulations, where the higher shear environments have lower maximum *w*. The sequence of maximum *w* between boundary-parallel vertical shear environments is not monotonic, indicating that the impact of the boundary-parallel vertical wind shear may depend on the initial θ' of the density current.

As the θ' goes beyond 7.0 K, the sequence of differences between boundary-parallel vertical wind shear environments are no longer clearly evident in the maximum *w* field. There is some separation (Figure 3.1 e,f,g); however, it is not distinguished as it is in θ' = 4.0 K and 5.0 K simulations. In simulations with θ' = 8.0 K, 9.0 K, and 10.0 K, some of the differences between boundary-parallel vertical wind shear environments are significant after a student *t*-test assessment (Table 3.1), but not nearly as many of the differences as there are in the θ' = 4.0 K through 7.0 K simulations. In θ' = 8.0 K and 9.0 K, the significant *t*-test results are generally negative, indicating higher shear favors

greater maximum *w*. However, the *t* statistics that are significant are generally small (all under 10.0). Therefore, it is difficult to make an argument that the boundary-parallel vertical wind shear has an impact on the maximum *w* of the three coldest boundaries simulated in this study.

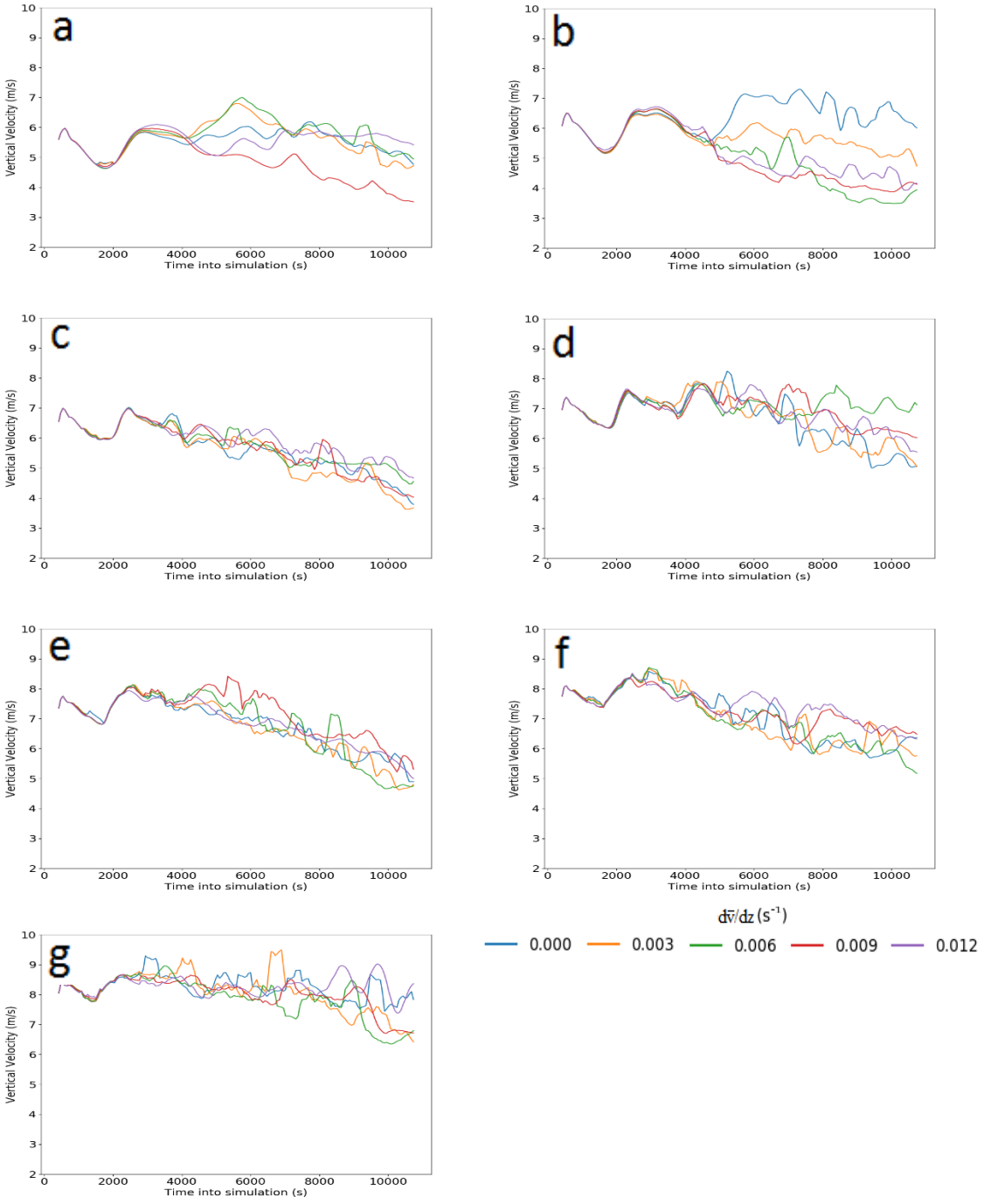

Figure 3.1: Maximum *w* time series from two dimensional simulations. Each panel represents one initial θ' : a.) 4.0 K b.) 5.0 K c.) 6.0 K d.) 7.0 K e.) 8.0 K f.) 9.0 K g.) 10.0 K

	4	5	6	7	8	9	10
0.000 – 0.012	-0.82 (0.41)	12.64 (< 1.00 x 10^{-3})	-7.72 (< 1.00 x 10^{-5})	-3.31 (1.03 x 10^{-3})	-1.86 (0.06)	-5.88 (< 1.00 x 10^{-5})	-0.70 (0.48)
0.000 – 0.009	13.32 (< 1.00 x 10^{-5})	13.39 (< 1.00 x 10^{-3})	-1.13 (0.26)	-4.79 (< 1.00 x 10^{-5})	-6.73 (< 1.00 x 10^{-5})	-3.49 (5.43 x 10^{-4})	3.75 (2.06 x 10^{-4})
0.003 – 0.012	1.43 (0.15)	9.13 (< 1.00 x 10^{-3})	-9.32 (< 1.00 x 10^{-5})	-3.07 (2.30 x 10^{-3})	-3.99 (8.00 x 10^{-5})	-5.99 (< 1.00 x 10^{-5})	-3.14 (1.83 x 10^{-3})
0.000 – 0.006	-8.04 (< 1.00 x 10^{-5})	12.77 (< 1.00 x 10^{-3})	-4.2 (3.00 x 10^{-5})	-5.53 (< 1.00 x 10^{-5})	-0.36 (0.72)	1.09 (0.27)	4.86 (< 1.00 x 10^{-5})
0.003 – 0.009	14.82 (< 1.00 x 10^{-5})	11.60 (< 1.00 x 10^{-3})	-3.6 (3.01 x 10^{-5})	-5.21 (< 1.00 x 10^{-5})	-8.49 (< 1.00 x 10^{-5})	-3.79 (1.77 x 10^{-4})	0.78 (0.45)
0.006 – 0.012	4.56 (< 1.00 x 10^{-5})	-3.53 (4.69 x 10^{-4})	-4.3 (2.20 x 10^{-5})	5.11 (< 1.00 x 10^{-5})	-0.73 (0.47)	-8.16 (< 1.00 x 10^{-5})	-6.14 (< 1.00 x 10^{-5})
0.000 – 0.003	-3.31 (1.03 x 10^{-3})	12.28 (< 1.00 x 10^{-5})	3.26 (1.22 x 10^{-3})	-0.44 (0.66)	1.96 (0.05)	0.61 (0.54)	2.42 (0.02)
0.003 – 0.006	-5.46 (< 1.00 x 10^{-5})	10.51 (< 1.00 x 10^{-5})	-6.73 (< 1.00 x 10^{-5})	-6.30 (< 1.00 x 10^{-5})	-1.93 (0.05)	0.36 (0.72)	2.47 (0.01)
0.006 – 0.009	14.60 (< 1.00 x 10^{-5})	0.78 (0.44)	2.77 (5.90 x 10^{-3})	3.11 (2.00 x 10^{-3})	-5.83 (< 1.00 x 10^{-5})	-5.02 (< 1.00 x 10^{-5})	-2.66 (8.16 x 10^{-3})
0.009 – 0.012	-12.49 (< 1.00 x 10^{-5})	-7.17 (< 1.00 x 10^{-5})	-6.26 (< 1.00 x 10^{-5})	2.25 (0.02)	6.66 (< 1.00 x 10^{-5})	-4.75 (< 1.00 x 10^{-5})	-5.45 (< 1.00 x 10^{-5})

Table 3.1: Results from the Student *t*-test on the maximum *w* field. Each row represents a difference between two boundary-parallel vertical shear environments. Each column is the initial θ' K of the airmass boundary. Green shaded is positive significant *t*-values. Red shaded is negative significant *t*-values. The associated *p* for each is in parenthesis.

Analyses of ascent depth and vertical displacement of passive-fluid tracers aid in quantifying the vertical extent of vertical motion and the amount of warm inflow air that is transported aloft. In simulations with θ' = 4.0 K, 2d-04-003 and 2d-04-006 have the greatest ascent depths at 1775 m and 1875 m, respectively (Figure 3.2a). Between 4000 and 6000 s, 2d-04-009 and 2d-04-012 ascent depth is only 1250 m and 1500 m, respectively. This makes for differences of over 300 m when comparing low shear environments to high shear environments during this time period of notable separation. Nine of ten differences in ascent depth between boundary-parallel shear environments are significant, with six of those nine having a *t* greater than 10.0 (Table 3.2). Examining tracer concentration just above the boundary, 2d-04-003 and 2d-04-006 values are 75% and 77% around the same time (Figure 3.3a). The maximum concentration values in 2d-04-009 and 2d-04-012 are 61% and 69%. Between 4000 and 5000 s, there is nearly a

20% difference between 2d-04-003 and 2d-04-012, as well as between 2d-04-003 and 2d-04-009. In the $\theta' = 4.0$ K tracer concentration field, nine of ten differences between boundary-parallel vertical shear environments are statistically significant, with eight of nine having *t* magnitudes greater than 10.0 (Table 3.3). Thus, these results are consistent as passive-fluid tracers should be expected to be lofted farther when vertical forcing is present through a greater depth. These results are consistent with the maximum *w* field, where 2d-04-003 and 2d-04-006 produce the greatest values and 2d-04-009 and 2d-04-012 the least.

In the $\theta' = 5.0$ K simulations, 2d-05-000 has the greatest ascent depth: 2025 m around 6100 s (Figure 3.2b). The shallowest maximum ascent depths are 1100 and 1250 m in 2d-05-009 and 2d-05-012. This is a difference of over 750 m between 2d-05-000 and the two highest shear environments. Nine of ten differences between shear environments in ascent depth are significant, with eight of nine having a *t* magnitude greater than 10.0 (Table 3.2). The analysis of tracer concentration reveals the same sequence between shear environments as ascent depth (Figure 3.3b). For example, around 7320 s, the 2d-05-000 concentration is at 79%, while the 2d-05-012 is lower with 54% concentration around the same time. The difference in tracer concentration between 2d-05-000 and 2d-05-012 is over 20% at multiple instances between 4000 and 7000 s, and above 15% between 4000 and 8000 s. In the passive-fluid tracer field, all differences between boundary-parallel vertical wind shear environments are significant for $\theta' = 5.0$ K. Eight of ten comparisons have a *t* of + 10.0 or greater (Table 3.3). As previously stated, deeper ascent depth with a greater amount of air lofted aligns

physically. Furthermore, the patterns in the maximum *w* analysis are congruent with the ascent depth and passive-fluid tracer analysis in the simulations with a $\theta' = 5.0$ K.

Similar to the maximum *w* analysis, the $\theta' = 4.0$ K and 5.0 K simulations display evident separation between boundary-parallel vertical wind shear environments for ascent depth and tracer transport. The $\theta' = 5.0$ K simulations demonstrate a sequence of shallower ascent depth and less tracer transport in higher shear environments, with deeper depth and greater transport in lower shear. The sequence is not monotonic in $\theta' = 4.0$ K, however, the highest two shear environments are the lowest two values in both ascent depth and vertical tracer displacement. This is consistent with $\theta' = 5.0$ K simulations.

When the θ' is increased to 6.0 K, there is little separation and no evident sequence between boundary-parallel vertical shear environments in ascent depth and passive-fluid tracer fields (Figures 3.2c & 3.3c). However, nine of ten comparisons are statistically significant in both fields after the *t*-test assessment (Table 3.2 & 3.3). This is similar to the analysis of maximum *w* in the simulations with a $\theta' = 6.0$ K. Despite the statistical significance, the lack of clear separation and sequence between shear environments makes it difficult to assert the existence of robust differences that describe the impacts on CI potential by altering the boundary-parallel vertical wind shear when the $\theta' = 6.0$ K.

When the θ' is increased to 7.0 K, notable separation between shear environments does appear around 7000 s in the ascent depth field (Figure 3.2d), similar to the sequence of the maximum *w* field. The shallowest ascent depths occur with 2d-07-000 and 2d-07-003, 1400 m and 1500 m, respectively. This is opposite of the $\theta' = 5.0$ K simulations, for which the two lowest shear environments are associated with the *greatest* ascent depths

and the *largest* maximum *w*. This sequence is not monotonic for the higher shear environments with $\theta' = 7.0$ K. The greatest ascent depth occurs with 2d-07-006. However, 2d-07-006, 2d-07-009, and 2d-07-012 all have a greater ascent depth than either 2d-07-000 or 2d-07-003. Thus, it can be concluded that the lowest two shear environments produce the shallowest maximum ascent depths, while the three higher shear environments are associated with greater ascent depth. The differences between boundary-parallel vertical wind shear environments are statistically significant, with *t* magnitudes between 6.85 and 12.80 (Table 3.2). Seven of ten computed *t*-statistics are negative, indicating a greater ascent depth is generally favored in the higher shear environments when $\theta' = 7.0$ K. However, unlike the smaller θ' simulations, the tracer displacement analysis of $\theta' = 7.0$ K simulations (Figure 3.3d) does not exhibit a clear reversal in the sequence as occurred in ascent depth and maximum *w*. Simulation 2d-07-006 is the outlier with a tracer maximum concentration just above 70% around 9000 s, while the other simulations did not exhibit substantial separation or a comparable sequence between low and high shear environments. Nine of ten differences in the tracer analysis at $\theta' = 7.0$ K are significant, but only two of the nine are characterized by *t* magnitudes greater than 10.0 (Table 3.3).

In simulations with a $\theta' = 8.0$ K and 9.0 K, there is some separation between boundary-parallel vertical shear environments in the ascent depth field from about 6000 s through the end of the simulations (Figure 3.2e,f). While the sequence is not monotonic, the lowest three shear environments are associated with the three shallowest ascent depths. The highest two shear environments are associated with the two greatest ascent depths. In the $\theta' = 8.0$ K simulations, the difference between the lower shear and high

shear environments is ~250 m. In the $\theta' = 9.0$ K simulations, the difference is nearly 500 m between 7000 and 9000 s. In both the $\theta' = 8.0$ K and 9.0 K simulations, nine of ten differences are significant (Table 3.2) and generally negative, indicating a greater ascent depth with higher boundary-parallel vertical wind shear. Similar to $\theta' = 7.0$ K, analysis of passive-fluid tracers in $\theta' = 8.0$ K and 9.0 K simulations show generally small and difficult to discern separation between shear environments (*t*-values generally < 10), and have no evident sequence between low vs. high shear (Figure 3.3e,f). When the θ' is increased to 10.0 K, both ascent depth and tracer analysis do not demonstrate clear separation or sequences between boundary-parallel vertical wind shear environments (Figure 3.2g & 3.3g). Despite statistical significance (Table 3.3), the lack of notable separation and/or a clear sequence in the time series plots between shear environments makes it difficult to use the tracer analysis alone to argue the impacts on CI potential that are attributable to changes in the boundary-parallel vertical wind shear.

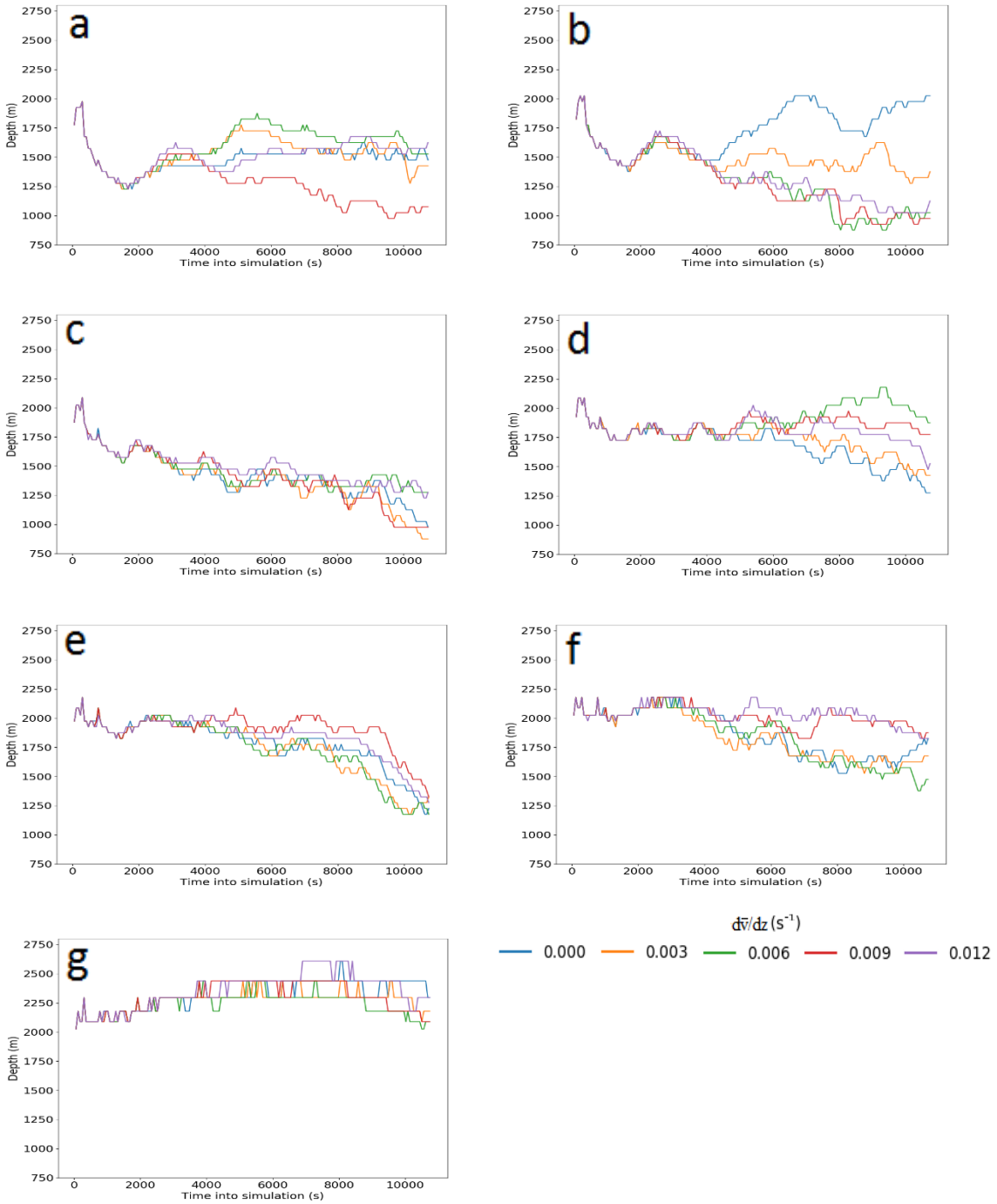

Figure 3.2: Ascent depth time series from two dimensional simulations. Each panel represents one initial θ' : a.) 4.0 K b.) 5.0 K c.) 6.0 K d.) 7.0 K e.) 8.0 K f.) 9.0 K g.) 10.0 K

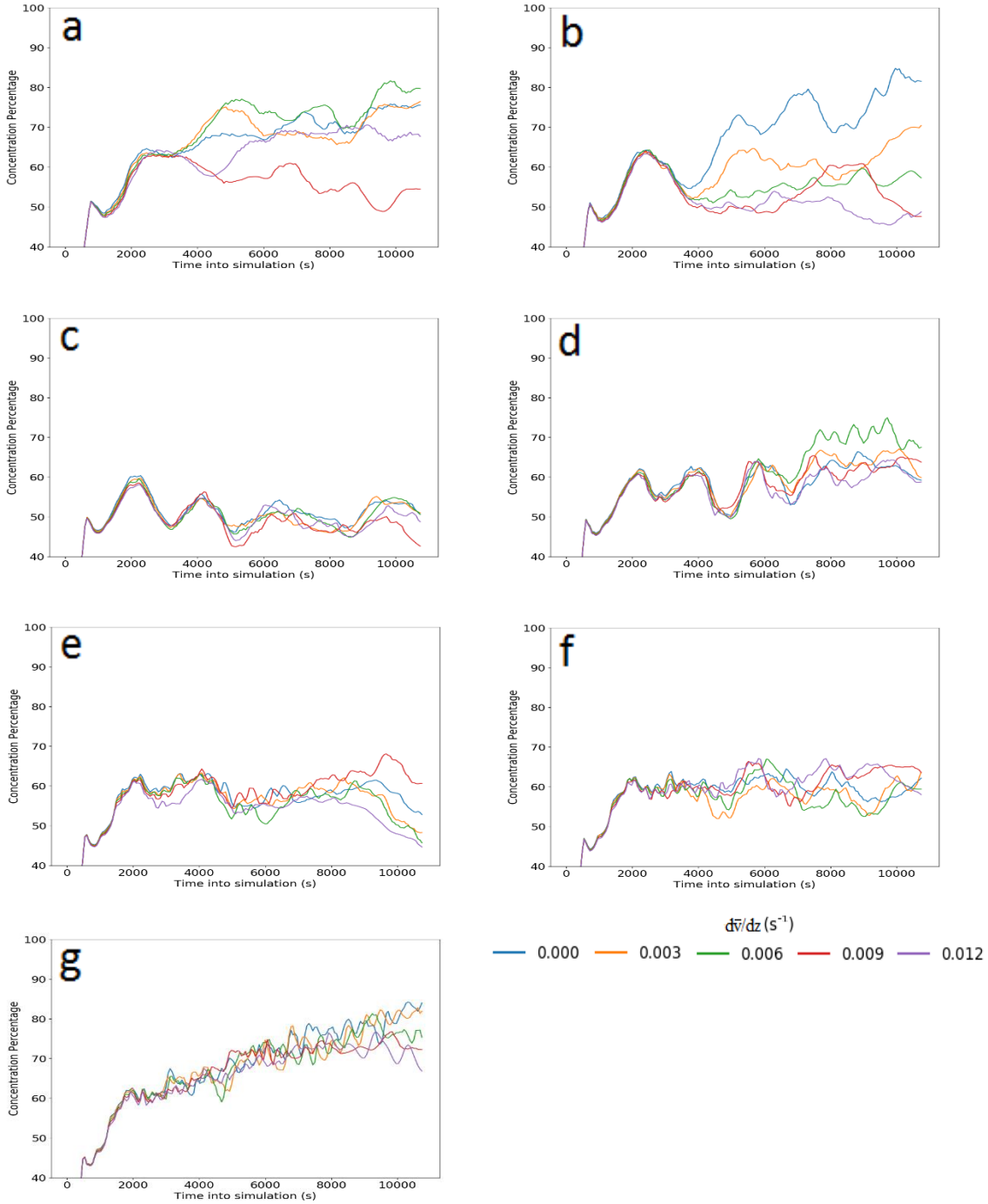

Figure 3.3: Passive-fluid tracer concentration above the density current head time series from two dimensional simulations. Each panel represents one initial θ' : a.) 4.0 K b.) 5.0 K c.) 6.0 K d.) 7.0 K e.) 8.0 K f.) 9.0 K g.) 10.0 K

	4	5	6	7	8	9	10
0.000 – 0.012	-7.09 (< 1.00 x 10^{-5})	13.67 (< 1.00 x 10^{-5})	-12.45 (< 1.00 x 10^{-5})	-12.80 (< 1.00 x 10^{-5})	-11.27 (< 1.00 x 10^{-5})	-12.75 (< 1.00 x 10^{-5})	-5.46 (< 1.00 x 10^{-5})
0.000 – 0.009	12.27 (< 1.00 x 10^{-5})	14.36 (< 1.00 x 10^{-5})	1.36 (0.17)	-12.59 (< 1.00 x 10^{-5})	-13.45 (< 1.00 x 10^{-5})	-12.12 (< 1.00 x 10^{-5})	2.18 (0.03)
0.003 – 0.012	1.19 (0.23)	11.09 (< 1.00 x 10^{-5})	-12.98 (< 1.00 x 10^{-5})	-10.77 (< 1.00 x 10^{-5})	-11.76 (< 1.00 x 10^{-5})	17.19 (< 1.00 x 10^{-5})	-10.54 (< 1.00 x 10^{-5})
0.000 – 0.006	-15.60 (< 1.00 x 10^{-5})	14.17 (< 1.00 x 10^{-5})	-6.83 (< 1.00 x 10^{-5})	-11.29 (< 1.00 x 10^{-5})	7.35 (< 1.00 x 10^{-5})	2.98 (3.08 x 10^{-3})	8.85 (< 1.00 x 10^{-5})
0.003 – 0.009	14.95 (< 1.00 x 10^{-5})	12.60 (< 1.00 x 10^{-5})	-3.60 (3.63 x 10^{-4})	-11.35 (< 1.00 x 10^{-5})	-12.78 (< 1.00 x 10^{-5})	-16.38 (< 1.00 x 10^{-5})	-3.96 (9.00 x 10^{-5})
0.006 – 0.012	8.11 (< 1.00 x 10^{-5})	-6.99 (< 1.00 x 10^{-5})	-7.37 (< 1.00 x 10^{-5})	7.99 (< 1.00 x 10^{-5})	-12.43 (< 1.00 x 10^{-5})	-14.15 (< 1.00 x 10^{-5})	-13.73 (< 1.00 x 10^{-5})
0.000 – 0.003	-6.93 (< 1.00 x 10^{-5})	13.71 (< 1.00 x 10^{-5})	5.21 (< 1.00 x 10^{-5})	-11.30 (< 1.00 x 10^{-5})	6.34 (< 1.00 x 10^{-5})	5.53 (< 1.00 x 10^{-5})	7.15 (< 1.00 x 10^{-5})
0.003 – 0.006	-13.76 (< 1.00 x 10^{-5})	11.84 (< 1.00 x 10^{-5})	-7.55 (< 1.00 x 10^{-5})	-10.31 (< 1.00 x 10^{-5})	1.80 (0.07)	-1.22 (0.22)	5.90 (< 1.00 x 10^{-5})
0.006 – 0.009	15.84 (< 1.00 x 10^{-5})	1.16 (0.25)	4.97 (< 1.00 x 10^{-5})	6.85 (< 1.00 x 10^{-5})	-13.02 (< 1.00 x 10^{-5})	-12.31 (< 1.00 x 10^{-5})	-10.76 (< 1.00 x 10^{-5})
0.009 – 0.012	-13.92 (< 1.00 x 10^{-5})	-10.69 (< 1.00 x 10^{-5})	-10.27 (< 1.00 x 10^{-5})	7.23 (< 1.00 x 10^{-5})	10.15 (< 1.00 x 10^{-5})	-5.54 (< 1.00 x 10^{-5})	-8.19 (< 1.00 x 10^{-5})

Table 3.2: Results from the Student *t*-test on the ascent depth field. Each row represents a difference between two boundary-parallel vertical shear environments. Each column is the initial θ' K of the airmass boundary. Green shaded is positive significant *t*-values. Red shaded is negative significant *t*-values. The associated *p* for each is in parenthesis.

	4	5	6	7	8	9	10
0.000 – 0.012	12.95 (< 1.00 x 10^{-5})	16.57 (< 1.00 x 10^{-5})	15.34 (< 1.00 x 10^{-5})	8.06 (< 1.00 x 10^{-5})	13.51 (< 1.00 x 10^{-5})	-3.80 (1.70 x 10^{-4})	10.63 (< 1.00 x 10^{-5})
0.000 – 0.009	16.54 (< 1.00 x 10^{-5})	15.92 (< 1.00 x 10^{-5})	13.76 (< 1.00 x 10^{-5})	0.92 (0.36)	-5.91 (< 1.00 x 10^{-5})	-2.84 (4.77 x 10^{-3})	7.93 (< 1.00 x 10^{-5})
0.003 – 0.012	8.43 (< 1.00 x 10^{-5})	14.69 (< 1.00 x 10^{-5})	5.31 (< 1.00 x 10^{-5})	12.25 (< 1.00 x 10^{-5})	17.42 (< 1.00 x 10^{-5})	-8.52 (< 1.00 x 10^{-5})	8.01 (< 1.00 x 10^{-5})
0.000 – 0.006	-10.44 (< 1.00 x 10^{-5})	16.55 (< 1.00 x 10^{-5})	10.82 (< 1.00 x 10^{-5})	-7.91 (< 1.00 x 10^{-5})	9.31 (< 1.00 x 10^{-5})	8.27 (< 1.00 x 10^{-5})	5.77 (< 1.00 x 10^{-5})
0.003 – 0.009	16.49 (< 1.00 x 10^{-5})	11.00 (< 1.00 x 10^{-5})	7.62 (< 1.00 x 10^{-5})	5.19 (< 1.00 x 10^{-5})	-6.37 (< 1.00 x 10^{-5})	-8.78 (< 1.00 x 10^{-5})	5.00 (< 1.00 x 10^{-5})
0.006 – 0.012	14.05 (< 1.00 x 10^{-5})	13.34 (< 1.00 x 10^{-5})	6.52 (< 1.00 x 10^{-5})	11.47 (< 1.00 x 10^{-5})	7.72 (< 1.00 x 10^{-5})	-6.84 (< 1.00 x 10^{-5})	7.31 (< 1.00 x 10^{-5})
0.000 – 0.003	0.35 (0.73)	16.46 (< 1.00 x 10^{-5})	9.24 (< 1.00 x 10^{-5})	-4.50 (< 1.00 x 10^{-5})	3.99 (8.00 x 10^{-5})	8.65 (< 1.00 x 10^{-5})	3.42 (6.98 x 10^{-4})
0.003 – 0.006	-11.08 (< 1.00 x 10^{-5})	12.56 (< 1.00 x 10^{-5})	0.21 (0.83)	-7.80 (< 1.00 x 10^{-5})	9.70 (< 1.00 x 10^{-5})	-0.79 (0.43)	3.10 (2.09 x 10^{-3})
0.006 – 0.009	16.44 (< 1.00 x 10^{-5})	6.94 (< 1.00 x 10^{-5})	7.84 (< 1.00 x 10^{-5})	8.81 (< 1.00 x 10^{-5})	-9.25 (< 1.00 x 10^{-5})	-6.87 (< 1.00 x 10^{-5})	3.74 (2.14 x 10^{-4})
0.009 – 0.012	-13.31 (< 1.00 x 10^{-5})	6.17 (< 1.00 x 10^{-5})	-5.00 (< 1.00 x 10^{-5})	9.29 (< 1.00 x 10^{-5})	11.27 (< 1.00 x 10^{-5})	-1.34 (0.18)	5.23 (< 1.00 x 10^{-5})

Table 3.3: Results from the Student *t*-test on the passive-fluid tracer concentration field. Each row represents a difference between two boundary-parallel vertical shear environments. Each column is the initial θ' K of the airmass boundary. Green shaded is positive significant *t*-values. Red shaded is negative significant *t*-values. The associated *p* for each is in parenthesis.

In environments that favor deep convection, deep ascent, quantified using ascent depth and passive-fluid tracer displacement in our simulations, will favor CI as it implies there will be forcing capable of lifting parcels to the LFC. Our analysis of the maximum *w* and ascent depth indicates a diminished CI potential in high boundary-parallel vertical wind shear environments with smaller initial θ' density currents. Differences of 200 to 500 m in ascent depth, which occur in our simulations, could make a difference between CI occurrence and CI failure in a real convective environment. The passive-fluid tracer analysis also indicates diminished CI potential in high boundary-parallel vertical wind shear environments with smaller θ' airmass boundaries, for which warm-buoyant air is not lifted through a deep depth. Thus this lack of ascent reduces the potential for CI.

At θ' = 6.0 K, differences in sequence between boundary-parallel vertical wind shear environments are not observed in either ascent depth or passive-fluid tracer analysis. However, differences reappear when θ' is increased to 7.0 K and beyond with maximum *w* and the ascent depth. Further, the sequence between low vs. high boundary-parallel vertical wind shear environments is opposite of the sequence in small θ' boundaries. The higher boundary-parallel vertical shear environments demonstrate enhanced CI potential due to greater ascent at the boundaries with a larger initial θ'. Thus, the boundary-parallel vertical wind shear impacts on CI potential depend on the initial temperature of the density current. Although there is separation in the depth of ascent fields in the larger θ' boundary simulations, faster boundary propagation speed (compared to the smaller θ' boundaries) may result in a greater gust-front relative flow. This may mean that the passive-fluid tracers are rapidly transported rearward of the boundary before they can be transported vertically along the leading edge (boundary propagation

speed will be discussed in the following section). Despite the CI potential differences due to differing forced ascent, as indicated by the ascent depth, it is not realized in the actual transport of warm-moist air indicated in the passive-fluid tracer analysis.

b. Propagation Speed

Previous work reviewed in chapter 1 establishes an associative relationship between boundary propagation speed and vertical ascent, physically attributable to convergence and changes in the fluid extension term of the vertical pressure gradient force. In our simulations, this associative relationship exists, as well as associative relationships with maximum *w*, ascent depth, and density current head buoyancy. In this section these relationships will be examined, and an overview of propagation speed comparisons between boundary-parallel vertical wind shear environments are provided.

For a specific initial cold block θ', the sequence of separation between boundary-parallel vertical wind shear environments nearly parallels the results of maximum *w* and ascent depth. In θ' = 4.0 K and 5.0 K simulations, the lowest propagation speeds occur with the two highest shear environments, just as the lowest maximum *w* and ascent depth values do. At θ' = 6.0 K, propagation speed does not demonstrate an evident sequence in the separation between shear environments, similar to the other fields analyzed in the θ' = 6.0 K simulations. At θ' = 7.0 K, 8.0 K, and 9.0 K, the sequence changes to the lower shear environments favoring slower propagation speed, which are also the environments that change from favoring greater values in maximum *w* and ascent depth favoring lower values.

Pearson's correlation coefficients between propagation speed and the fields used as proxy for CI are in alignment with this assertion. Between propagation speed and

maximum *w* for all 35 simulations, r = 0.93 (Figure 3.4). Between propagation speed and ascent depth, r = 0.91 (Figure 3.5). For propagation speed and tracer concentration, r = 0.31 (Figure 3.6). Recall the sequences of boundary-parallel vertical wind shear environments between propagation speed, maximum *w*, ascent depth, and tracer concentration are similar in θ' = 4.0 K and 5.0 K simulations; however, the propagation speed sequence is only similar to maximum *w* and ascent depth for $\theta' \geq 7.0$ K while tracer concentration is not. For θ' = 4.0 and 5.0 K, r = 0.58 and r = 0.44 between tracer concentration and propagation speed, respectively, while r < 0.36 for simulations $\theta' \geq 7.0$ K. Thus, the overall correlation between propagation speed and tracer concentration is weak, while it is stronger between propagation speed, maximum *w*, and ascent depth. This is attributed to the strong gust-front relative flow in the larger initial θ' cold block boundaries, which swiftly move the tracers rearward before being transported vertically. Although not realized in all simulations in the passive-fluid tracers, the strong correlation between propagation speed, maximum *w*, and ascent depth add confidence to the large role propagation speed has in forced ascent along the leading edge. Based on these sequences and the physical consistency, we assert that propagation speed is largely driving maximum *w*, ascent depth, and to some extent, the tracer concentration in our simulations.

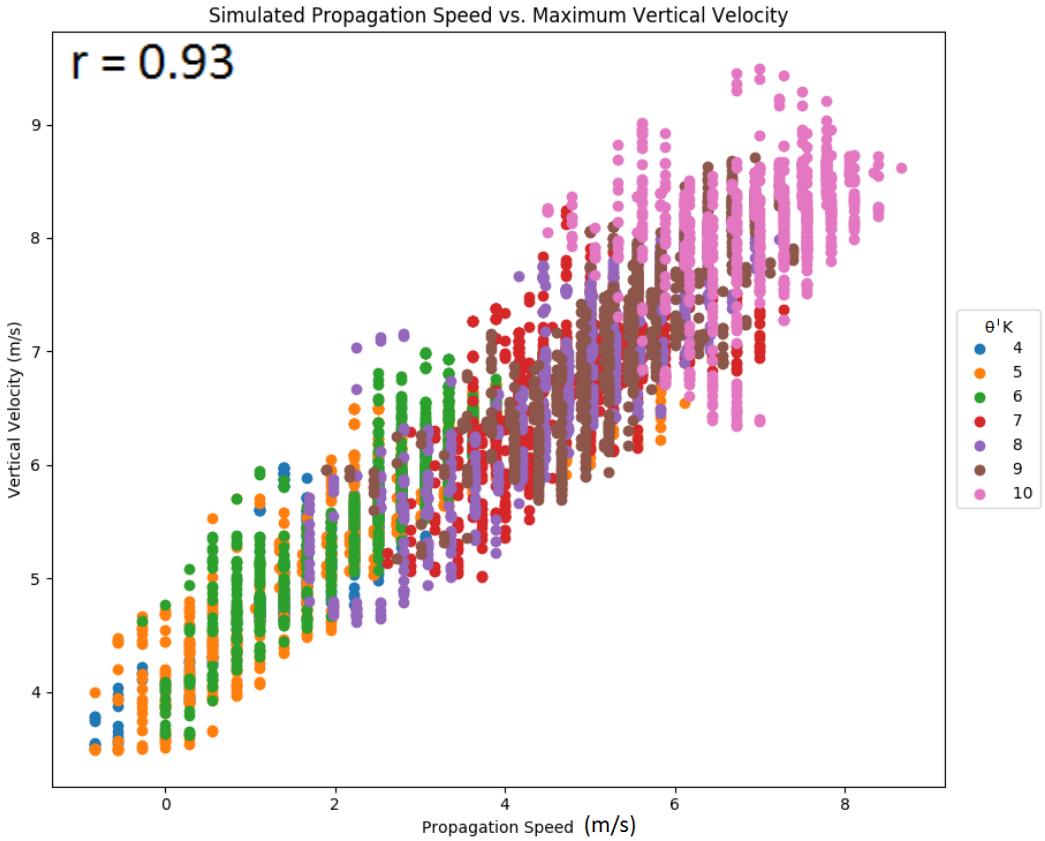

Figure 3.4: Boundary propagation speed vs. maximum *w*. Data points are from all 35 2D simulations, and include all times.

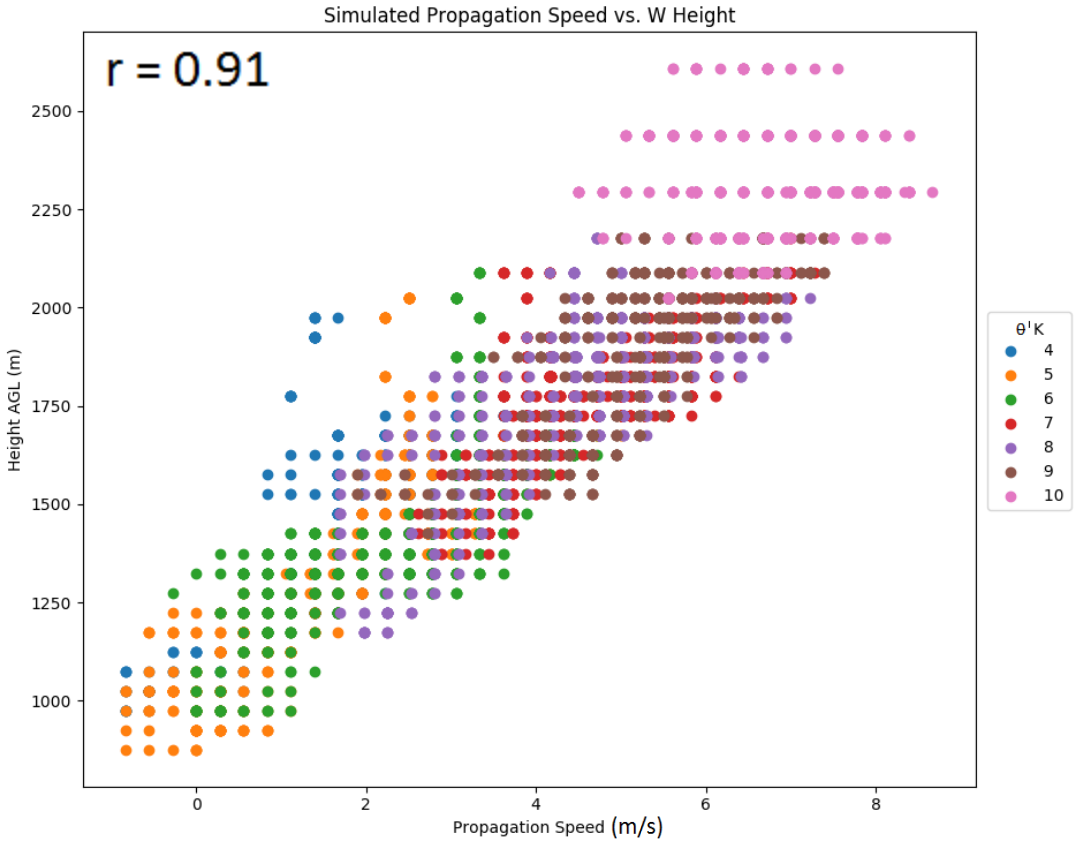

Figure 3.5: Boundary propagation speed vs. depth of vertical ascent. Data points are from all 35 2D simulations, and include all times.

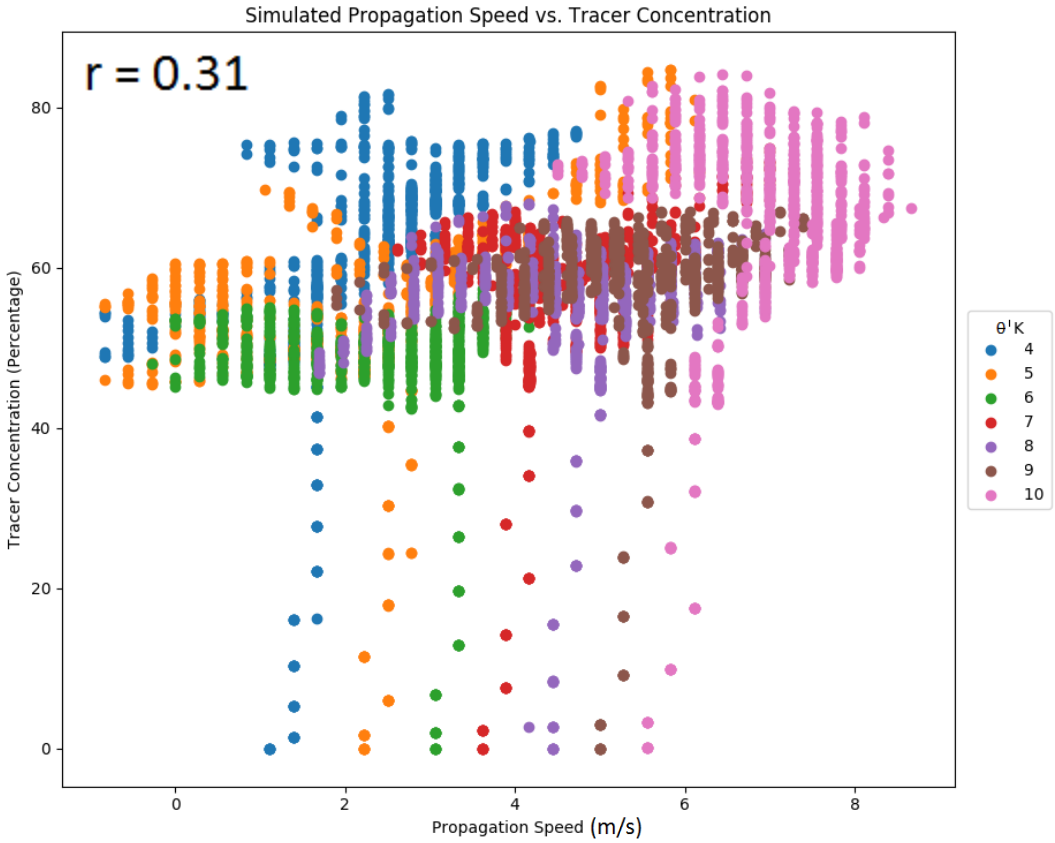

Figure 3.6: Boundary propagation speed vs. lofted tracer concentration. Data points are from all 35 2D simulations, and include all times.

The analysis of propagation speed reveals a strong associative relationship with forced ascent. To identify the mechanisms by which the boundary-parallel vertical shear impacts propagation speed it is necessary to determine what is controlling boundary propagation speed in these simulations. As reviewed in the introduction, previous work suggests that density current propagation speed is controlled by the density current buoyancy, and/or the density current head depth. Both buoyancy and the head depth controls propagation speed through the horizontal PGF developed between the density current and the ambient environment. A colder and/or deeper density current should be expected to propagate faster as the horizontal PGF will be greater. Examining buoyancy time series plots, the sequence of the shear environments in propagation speed and buoyancy largely match up appropriately. For example, between 5000 and 7000 s where the most notable separation in propagation speed between shear environments in the $\theta' = 4.0$ K and 5.0 K simulations occurs, the two highest shear environments are the slowest propagating and are not as negatively buoyant compared to their lower shear counterparts (Figure 3.7a,b). The negative, significant *t*-test results also show that the higher shear environments are associated with smaller θ' boundaries (Table 3.4 a,b). However, at $\theta' \geq 7.0$ K, the sequence in buoyancy changes, just as it does in propagation speed. The lower shear environments propagate slower, and are not as negatively buoyant as their higher shear counterparts (Figure 3.7d,e,f,g). This is generally captured in the student *t*-test results as well (Table 3.4d,e,f,g). Encompassing all simulations, propagation speed and buoyancy are well correlated, r = -0.86 (Figure 3.8). Thus, our simulations appear to reveal that buoyancy has control over the propagation speed of the boundary, while in turn the propagation speed regulates forced ascent along the leading edge.

Previous studies on flow-force balance reveal that density current propagation speed is also sensitive to the density current depth as a result of hydrostatic pressure responses. Greater density current depths are associated with faster propagation speeds. In our simulations, this holds true when examining the time series plots (Figure 3.9) and the student *t*-test analysis (Table 3.4). The simulations with faster propagating boundaries are also the simulations with deeper density current head depths. As the initial θ' becomes colder, both propagation speed and density current head depth show a reversal in the sequence between boundary-parallel vertical shear environments. However, propagation speed and density current head depth are not as well correlated as propagation speed and buoyancy, with r = 0.62 (Figure 3.10). Although the time series and *t*-test indicate an apparent associative relationship between propagation speed and head depth in our simulations, the weaker correlation may be an indication that changes in head depth are not driving changes in propagation speed. Analysis of a theoretical propagation speed may be able provide further insight.

Figure 3.7: Density current buoyancy time series from two dimensional simulations. Each panel represents one initial θ' : a.) 4.0 K b.) 5.0 K c.) 6.0 K d.) 7.0 K e.) 8.0 K f.) 9.0 K g.) 10.0 K

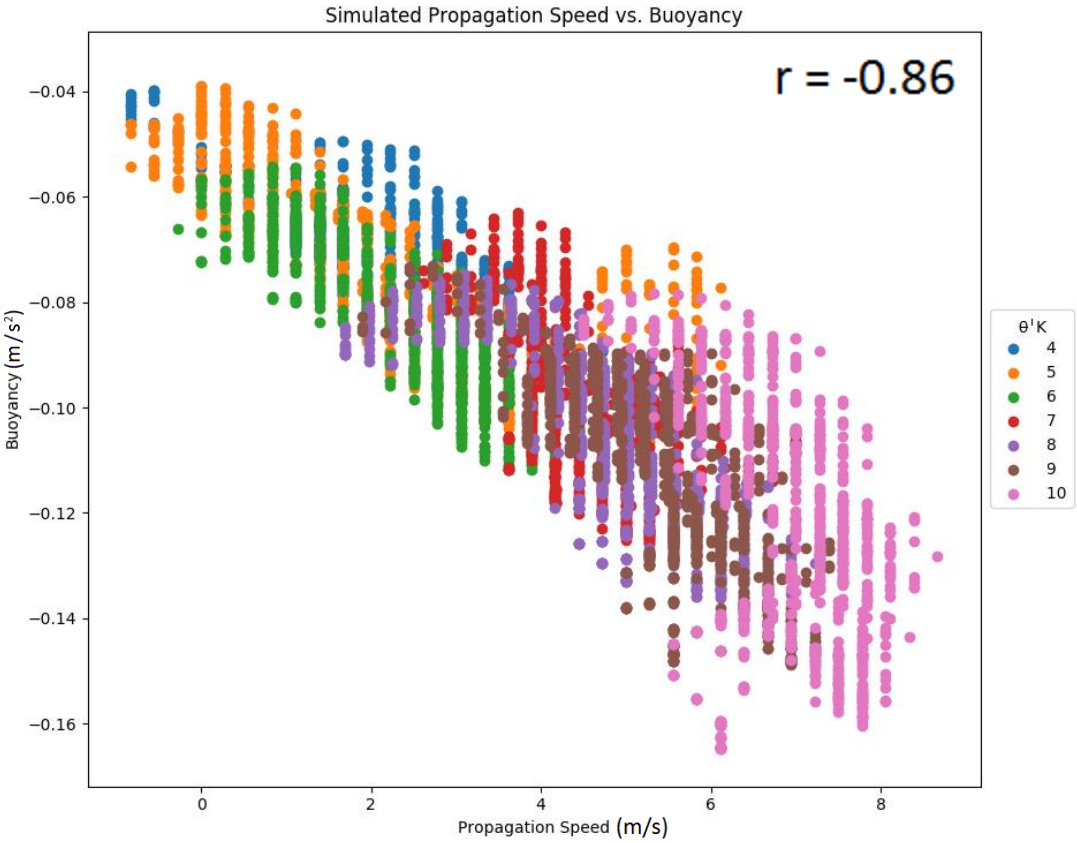

Figure 3.8: Propagation speed vs. buoyancy. This includes all 35 2D simulations, and encompasses all times.

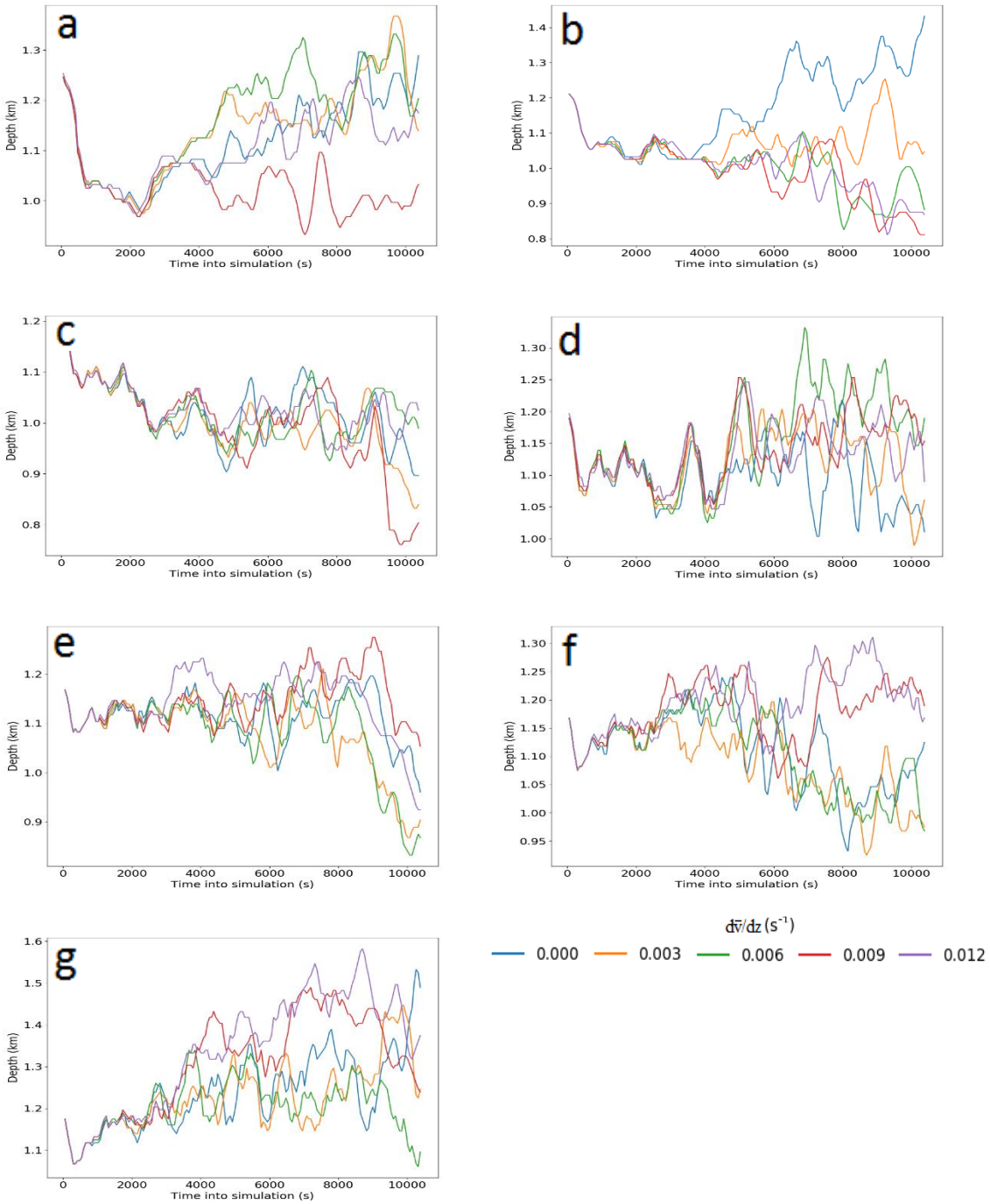

Figure 3.9: Density current head depth time series from two dimensional simulations. Each panel represents one initial θ' : a.) 4.0 K b.) 5.0 K c.) 6.0 K d.) 7.0 K e.) 8.0 K f.) 9.0 K g.) 10.0 K

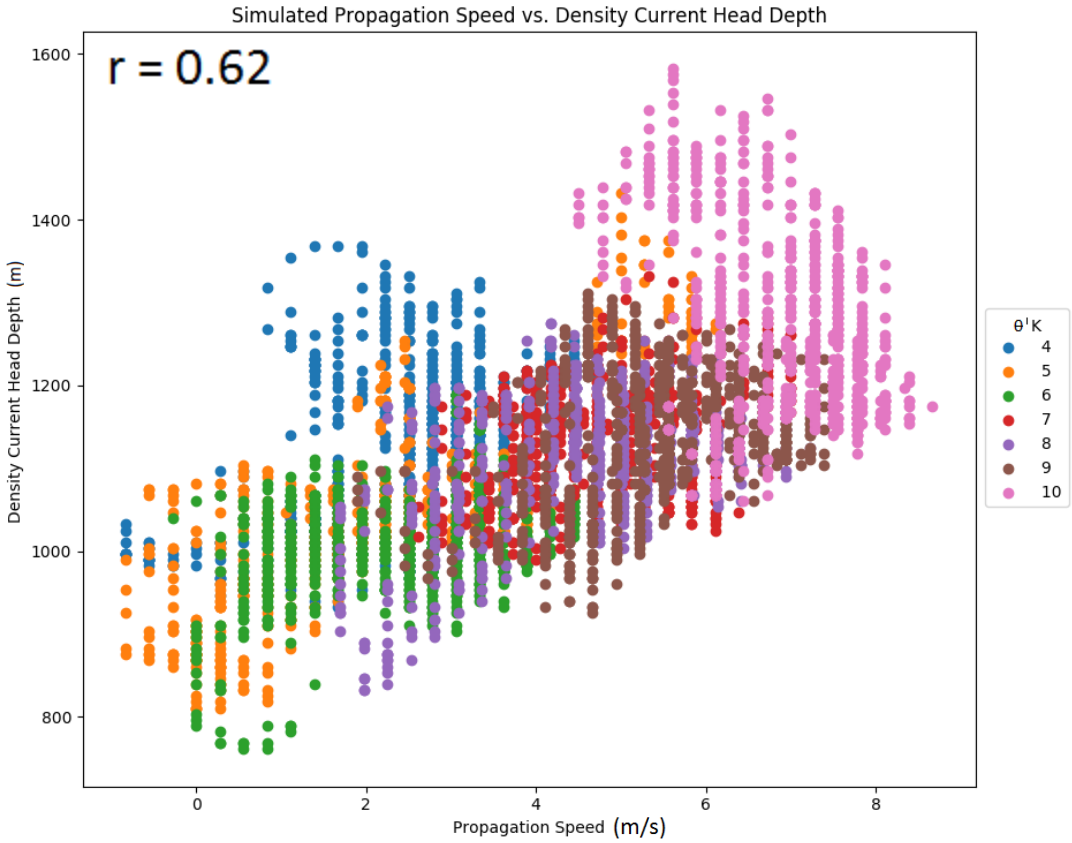

Figure 3.10: Density current head depth vs. boundary propagation speed. All 2D simulations and all time points are included.

a Initial Cold Block -4.0 K	Maximum Vertical Velocity	Vertical Velocity Height	Tracer Concentration	Propagation Speed	Head Depth	Buoyancy	Gust-Front Relative Winds	Pressure Perturbation
0.000 - 0.012	-	-	+	+	+	+	-	+
0.000 - 0.009	+	+	+	+	+	-	+	+
0.003 - 0.012	+	+	+	+	+	+	-	+
0.000 - 0.006	-	-	-	-	-	+	-	-
0.003 - 0.009	+	+	+	+	+	-	+	+
0.006 - 0.012	+	+	+	+	+	+	+	+
0.000 - 0.003	-	-	-	+	-	+	-	-
0.003 - 0.006	-	-	-	-	-	+	-	-
0.006 - 0.009	+	+	+	+	+	-	+	+
0.009 - 0.012	-	-	-	-	-	+	-	-

b Initial Cold Block -5.0 K	Maximum Vertical Velocity	Vertical Velocity Height	Tracer Concentration	Propagation Speed	Head Depth	Buoyancy	Gust-Front Relative Winds	Pressure Perturbation
0.000 - 0.012	+	+	+	+	+	-	+	+
0.000 - 0.009	+	+	+	+	+	-	+	-
0.003 - 0.012	+	+	+	+	+	-	+	+
0.000 - 0.006	+	+	+	+	+	-	+	-
0.003 - 0.009	+	+	+	+	+	-	+	+
0.006 - 0.012	-	-	+	-	+	+	-	-
0.000 - 0.003	+	+	+	+	+	-	+	-
0.003 - 0.006	+	+	+	+	+	-	+	-
0.006 - 0.009	+	+	+	+	+	+	-	-
0.009 - 0.012	-	-	+	-	-	+	-	-

c Initial Cold Block -6.0 K	Maximum Vertical Velocity	Vertical Velocity Height	Tracer Concentration	Propagation Speed	Head Depth	Buoyancy	Gust-Front Relative Winds	Pressure Perturbation
0.000 - 0.012	-	-	+	-	-	+	-	+
0.000 - 0.009	-	+	+	+	+	+	-	-
0.003 - 0.012	-	-	+	-	-	+	-	+
0.000 - 0.006	-	-	+	-	-	+	-	+
0.003 - 0.009	-	-	+	-	+	+	-	+
0.006 - 0.012	-	-	+	-	-	+	-	+
0.000 - 0.003	+	+	+	+	+	-	+	-
0.003 - 0.006	-	-	+	-	-	+	-	+
0.006 - 0.009	+	+	+	+	+	-	+	-
0.009 - 0.012	-	-	-	-	-	+	-	+

d Initial Cold Block -7.0 K	Maximum Vertical Velocity	Vertical Velocity Height	Tracer Concentration	Propagation Speed	Head Depth	Buoyancy	Gust-Front Relative Winds	Pressure Perturbation
0.000 - 0.012	-	-	+	-	-	+	-	+
0.000 - 0.009	-	-	+	-	-	+	-	+
0.003 - 0.012	-	-	+	-	-	+	-	+
0.000 - 0.006	-	-	-	-	-	+	-	+
0.003 - 0.009	-	-	+	-	-	+	-	+
0.006 - 0.012	+	+	+	+	+	-	+	-
0.000 - 0.003	-	-	-	-	-	+	-	+
0.003 - 0.006	-	-	-	-	-	+	-	+
0.006 - 0.009	+	+	+	+	+	-	+	-
0.009 - 0.012	+	+	+	+	+	-	-	-

e Initial Cold Block -8.0 K	Maximum Vertical Velocity	Vertical Velocity Height	Tracer Concentration	Propagation Speed	Head Depth	Buoyancy	Gust-Front Relative Winds	Pressure Perturbation
0.000 - 0.012	-	-	+	+	-	-	-	-
0.000 - 0.009	-	-	-	-	-	+	-	+
0.003 - 0.012	-	-	+	+	-	-	-	-
0.000 - 0.006	-	+	+	+	+	+	+	-
0.003 - 0.009	-	-	-	-	-	+	-	+
0.006 - 0.012	-	-	+	+	-	-	-	-
0.000 - 0.003	+	+	+	+	+	+	+	-
0.003 - 0.006	-	+	+	+	-	+	+	-
0.006 - 0.009	-	-	-	-	-	+	-	+
0.009 - 0.012	+	+	+	+	+	-	+	-

f Initial Cold Block -9.0 K	Maximum Vertical Velocity	Vertical Velocity Height	Tracer Concentration	Propagation Speed	Head Depth	Buoyancy	Gust-Front Relative Winds	Pressure Perturbation
0.000 - 0.012	-	-	-	-	-	+	-	+
0.000 - 0.009	-	-	-	-	-	-	-	+
0.003 - 0.012	-	+	-	-	-	-	-	+
0.000 - 0.006	+	+	+	+	+	-	-	-
0.003 - 0.009	-	-	-	-	-	-	-	+
0.006 - 0.012	-	-	-	-	-	+	-	+
0.000 - 0.003	+	+	+	+	+	+	+	-
0.003 - 0.006	+	-	-	+	-	-	-	-
0.006 - 0.009	-	-	-	-	-	+	-	+
0.009 - 0.012	-	-	-	-	-	+	-	+

g Initial Cold Block -10.0 K	Maximum Vertical Velocity	Vertical Velocity Height	Tracer Concentration	Propagation Speed	Head Depth	Buoyancy	Gust-Front Relative Winds	Pressure Perturbation
0.000 - 0.012	-	-	+	+	-	-	-	-
0.000 - 0.009	+	+	+	+	-	-	-	-
0.003 - 0.012	-	-	+	+	-	-	-	-
0.000 - 0.006	+	+	+	+	+	-	+	-
0.003 - 0.009	+	-	+	+	-	-	-	-
0.006 - 0.012	-	-	+	+	-	-	-	-
0.000 - 0.003	+	+	+	+	+	-	-	-
0.003 - 0.006	+	+	+	+	+	+	+	-
0.006 - 0.009	-	-	+	+	-	-	-	-
0.009 - 0.012	-	-	+	-	-	-	-	+

Table 3.4: Results from the Student t-test on the fields analyzed in the 2D simulations. Cells filled with a color represent significant t-values (+/- 2.6). Each table represents one initial θ' : a.) 4.0 K b.) 5.0 K c.) 6.0 K d.) 7.0 K e.) 8.0 K f.) 9.0 K g.) 10.0 K

The von Karman (1940) equation for density current speed is used to calculate a theoretical propagation speed, based on density current buoyancy and depth from our simulations.

$$C^2 = -2\int_0^h B\, dz \quad (1)$$

This equation provides a means to separate buoyancy (B) and head depth (h), as these are explicitly accounted for in the equation. Ultimately, it is used to reveal which one exerts more control over propagation speed (C). While vertical wind shear is not explicitly accounted for in (1), it is implicitly captured through the inclusion of buoyancy and head depth, because our results indicate that there is sensitivity in both of these fields to the boundary-parallel vertical wind shear. First, C is calculated from (1) using the

buoyancy and head depth values from our simulations, to ensure consistency with the propagation speed from the simulations. Overall, the von Karman (1940) calculations are consistent with the sequence between boundary-parallel vertical wind shear environments as occurs in the propagation speed from the simulations. For example, in $\theta' = 5.0$ K, both the simulated and von Karman (1940) propagation speeds have 2d-05-000 as the fastest, with 2d-05-009 and 2d-05-012 the slowest (Figure 3.11a). The separation between the low and high shear environments is ~5.5 m s^{-1} in both the simulated and theoretical values. Then at $\theta' = 7.0$ K, this changes to 2d-07-000 being slower than 2d-07-009 and 2d-07-012 in both the simulated propagation speed and the calculated von Karman (1940) values (Figure 3.11b). The separation between the low and high shear environments is ~3.5 m s^{-1} in both the simulated and theoretical propagation speeds. Thus, by using the buoyancy and head depth values from our simulations, the von Karman (1940) theoretical and our simulated propagation speeds have comparable sequences.

In the next set of von Karman (1940) calculations, the buoyancy is held constant with the initialization value (t = 0). The head depth values are the values that occur in the simulations. This allows us to see how propagation speed responds to changes in head depth. In the von Karman (1940) time series plots of $\theta' = 5.0$ K simulations where buoyancy is held constant, 2d-05-000 is the fastest, while 2d-05-009 and 2d-05-012 are the slowest (Figure 3.11c) just as is the case in the simulations. However, the greatest separation between the low and high shear environments is less than 2.0 m s^{-1}, where in the simulated propagation speed this is closer to 5.5 m s^{-1}. In $\theta' = 7.0$ K simulations, the theoretical propagation speed sequence of shear environments is also the same as the simulated propagation speed sequence, where 2d-07-000 is slower than 2d-07-009 and

2d-07-012 (Figure 3.11d). However, the separation is at most 1.0 m s^{-1}, where in the simulated propagation speed this is closer to 3.5 m s^{-1}. Despite a suggested associative relationship apparent between the simulated propagation speed and head depth, the weak correlation is an indicator that changes in head depth are not driving the robust changes in propagation speed. Further, the lack of robust separation in this set of von Karman (1940) calculations also supports this argument, as these values should be closer to the actual propagation speed if head depth is largely driving it.

The final set of von Karman (1940) calculations hold head depth constant, using the simulated head depth of the density current at initialization. The values of buoyancy within the density current head from the simulations are used. This allows us to see how the propagation speed responds to changes in buoyancy. In the von Karman (1940) time series plots, where head depth is held constant, the sequence between boundary-parallel vertical wind shear environments is the same as the simulated propagation speed. For example, in the θ' = 5.0 K simulations, 2d-05-000 is the fastest while 2d-05-009 and 2d-05-012 are the slowest (Figure 3.11e). The separation between the low and high shear environments is ~5.0 m s^{-1}, similar to the 5.5 m s^{-1} separation in the simulated propagation speed. At θ' = 7.0 K, the sequence changes, where 2d-07-000 is slower than 2d-07-009 and 2d-07-012 (Figure 3.11f). The separation between the low and high shear environments is ~3.0 m s^{-1}, similar to the ~3.5 m s^{-1} separation in the simulated propagation speed. Not only is the sequence between shear environments the same in these theoretical von Karman (1940) calculations, the magnitude of the differences are also comparable. Recall that the sequence of boundary-parallel vertical shear environments in simulated propagation speed and buoyancy are similar. Additionally, the

simulated values of propagation speed and buoyancy are well correlated. Thus, these von Karman (1940) calculations showing similar differences in theoretical propagation speed when buoyancy is altered are consistent with the values of the simulated propagation speed and buoyancy. Thus, with these robust differences in both the simulated and theoretical values, it appears that buoyancy is largely driving the propagation speed of density currents in our simulations. The next question to explore is how the boundary-parallel vertical wind shear physically influences the buoyancy and propagation speed.

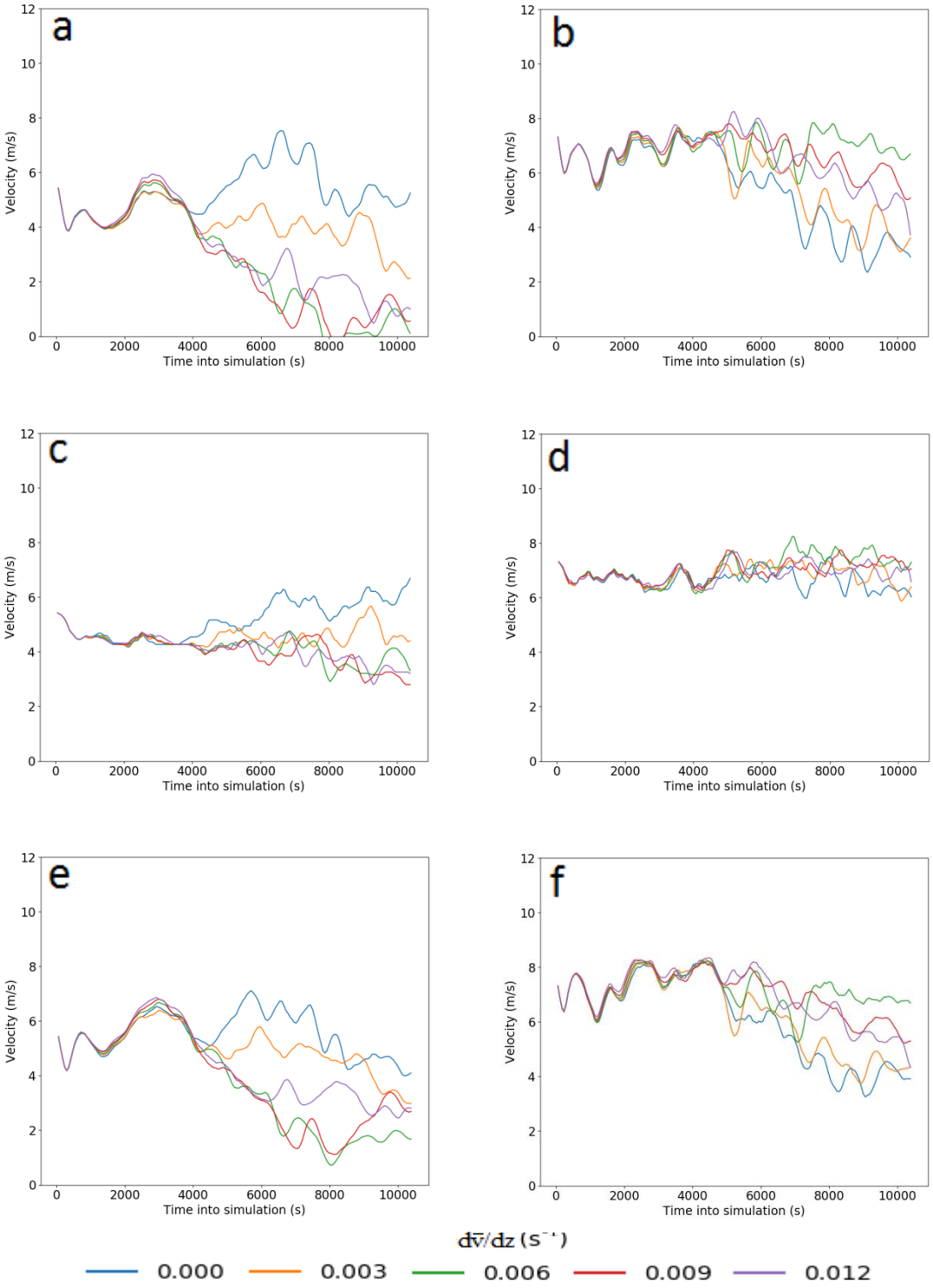

Figure 3.11: Time series of propagation speed via the von Karman (1940) equation. Each panel is initial θ' : a.) 5.0 K b.) 7.0 K c.) 5.0 K, buoyancy constant d.) 7.0 K, buoyancy constant e.) 5.0 K, head depth constant f.) 7.0 K, head depth constant

c. Physical Processes Sensitive to the Boundary-Parallel Vertical Wind Shear

Given that there is notable sensitivity to both changes in the boundary-parallel vertical wind shear and the initial θ' of the cold block, indicated by a reversal in the sequence, there may be multiple processes that are altering the density current buoyancy and, subsequently, propagation speed and forced ascent as the sequences become opposite when the initial θ' is larger. First, θ' = 4.0 and 5.0 K simulations will be examined. These are the simulations in which CI potential is favored in the lower shear environments, and diminished in higher shear environments. Recall, in both θ' = 4.0 K and 5.0 K between 4000 and 7000 s, the two highest boundary-parallel vertical wind shear environments are the least negatively buoyant simulations. The lower shear environments are colder, or more negatively buoyant. The higher boundary-parallel vertical shear environments should theoretically promote greater mechanical mixing. As a result of greater mixing, the density current head should ingest warmer air from the ambient environment at a greater rate than the lower shear environments. In x-z plots of passive-fluid tracer, this mixing process is evident. For example in the θ' = 5.0 K simulations between 4000 and 6000 s, 2d-05-000 retains a larger area of tracers less than 15% concentration within the head than 2d-05-012 (Figure 3.12) (recall 100% tracer concentration represents pure warm ambient air from the lowest 750 m). In 2d-05-012, tracer concentration in excess of 45% is present in much of the head. Thus, in 2d-05-000 there is more cold outflow air remaining inside the head, where 2d-05-012 takes in warmer air. As a result of taking in warmer air and becoming less negatively buoyant, the higher shear environments are decreasing the horizontal pressure gradient force between

the boundary and ambient environment, reducing the propagation speed and subsequent forced ascent along the leading edge of the boundary.

At $\theta' \geq 7.0$ K, the sensitivity to the boundary-parallel shear reverses: Lower shear environments are associated with the less negatively buoyant density currents, where the higher shear environments are colder, or more negatively buoyant. Thus, the process of higher shear promoting greater mixing and ingestion of warm air into the density current head does not hold in these larger θ' boundary simulations. This is likely attributable to the increased static stability of the larger θ' boundaries. With an increased static stability, the density current is much less likely to be influenced by mixing than the small θ' boundaries with lower static stability. Thus, despite the higher shear promoting greater mechanical mixing, the boundary is largely unaffected, and the higher shear environments do not make the boundary less negatively buoyant. However, given that the higher shear environments in general are associated with the more negatively buoyant boundaries, there must be another process that is facilitating this.

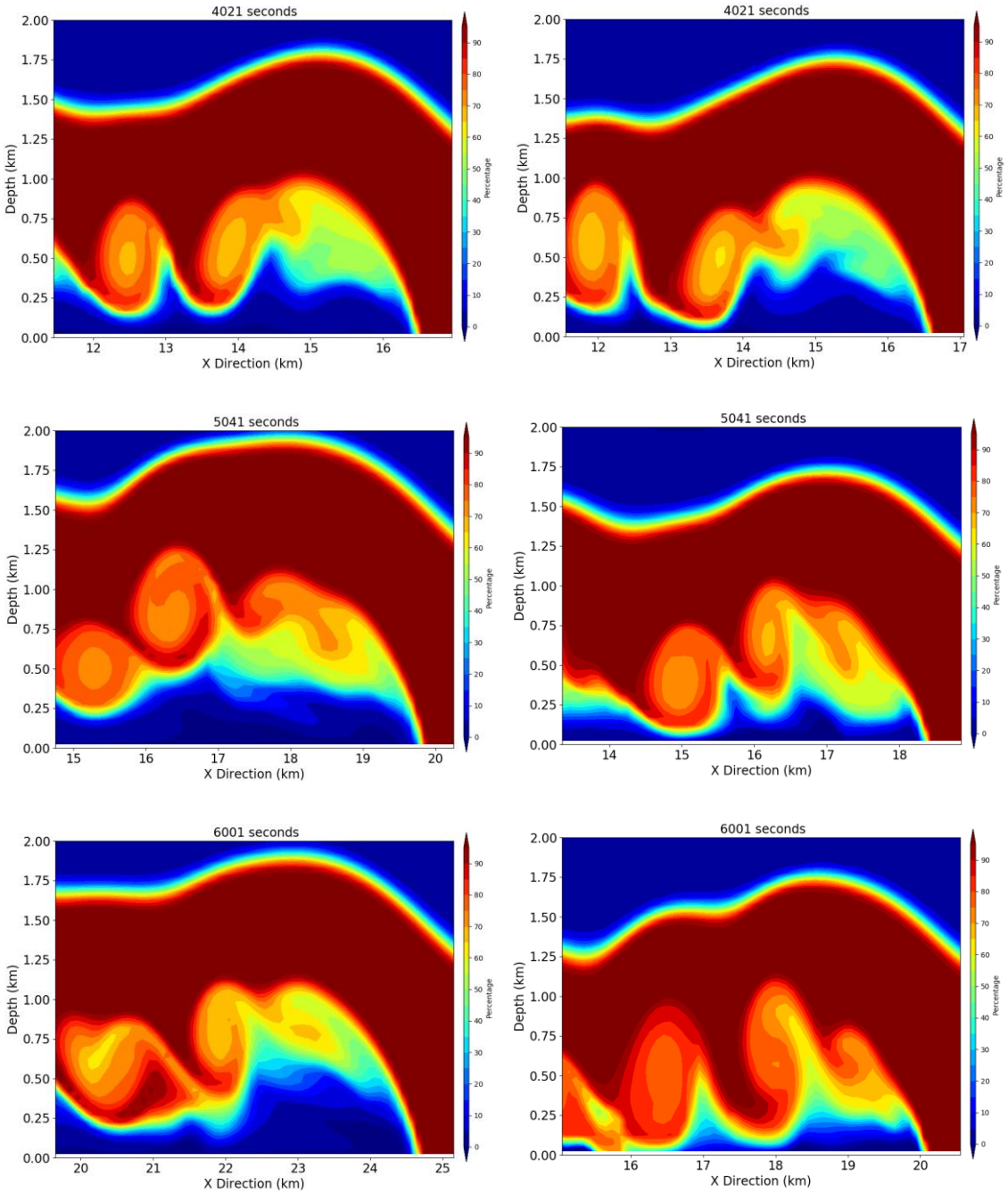

Figure 3.12: Tracer concentration. The left column is 2d-05-000 and the right column is 2d-05-012. Time increases from top to bottom.

Analysis of the passive-fluid tracer and gust-front relative *u*-wind reveals another process that affects the propagation speed. The first feature to make note of in the passive-fluid tracer plots is the development of KH billows, generated along the upper interface of the density current (Figure 3.12). As the KH billows develop and move downward, the gust-front relative winds undergo a substantial easterly increase beneath the KH gyre. Subsequently, this positive *u* acceleration continues into the head of the density current (Figure 3.13). This affects propagation speed in two ways: First, it provides positive-*u* momentum into the head, which accelerates the outflow boundary. Secondly, by advecting cold, negatively buoyant air beneath the gyre from the trailing cold air behind the wake, it also acts to accelerate the boundary through associated pressure increases.

The gust-front relative-*u* wind time series for $\theta' = 7.0$ K, 8.0 K, and 9.0 K reveal the lower shear environments are associated with the lower velocities, and higher shear with greater velocities (Figure 3.14). In general, after 6000 s, 0.000 s^{-1} and 0.003 s^{-1} are between 6 and 8 m s^{-1} and 0.009 s^{-1} and 0.012 s^{-1} are between 9 and 10 m s^{-1}. The student *t*-test results also demonstrate this same sequence, as significant values are negative (Table 3.4d,e,f). This aligns well with the simulated propagation speed analysis and the subsequent forced ascent. This is also consistent with density current head buoyancy results. The higher shear environments with greater gust-front relative-*u* winds into the head had more negative buoyancy than the lower shear environments.

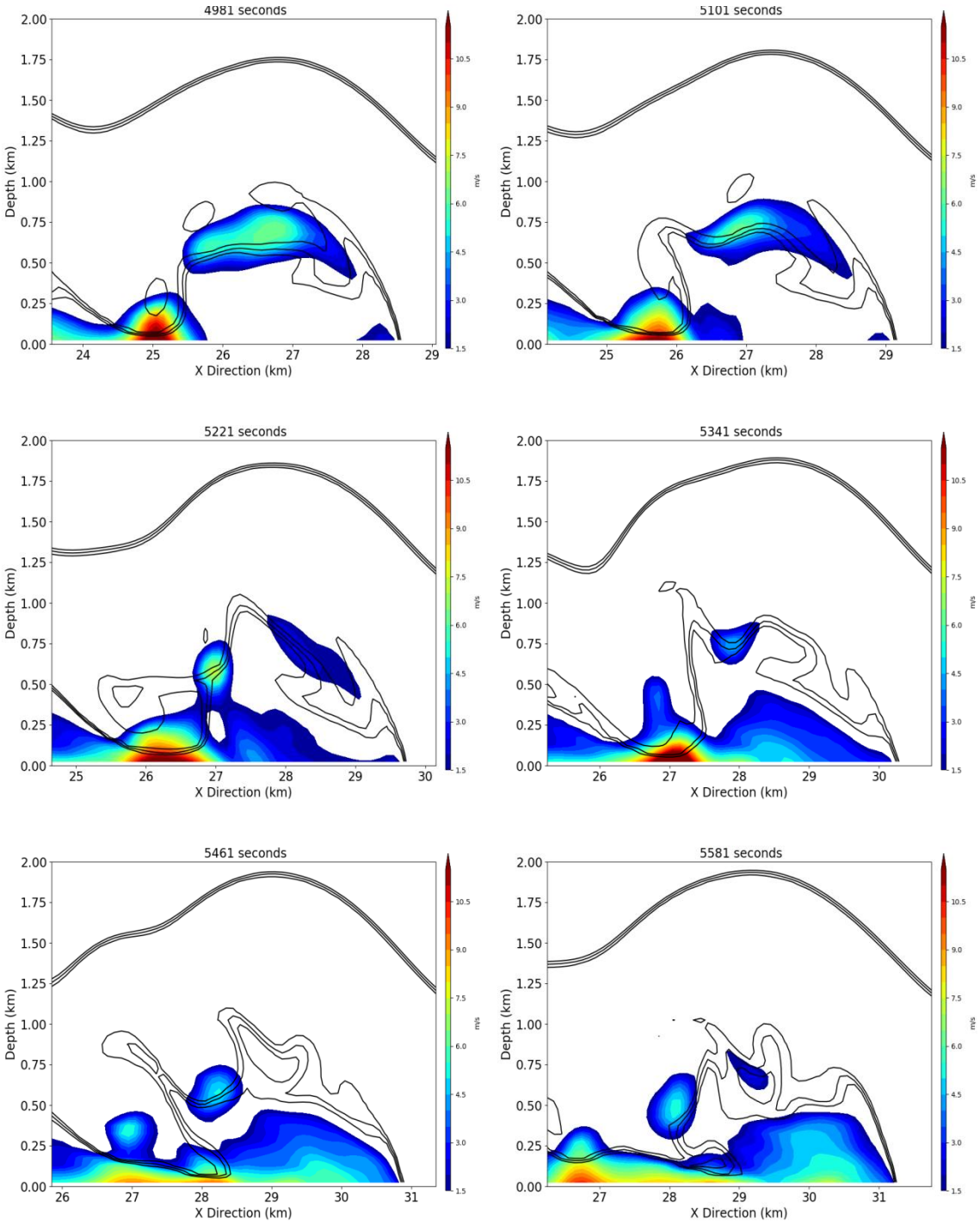

Figure 3.13: Time evolution of the easterly momentum pushes into the density current head as KH billows move downward. The color fill is the gust-front relative *u*-wind. The black lines represent tracer concentration to outline the density current and KH billows. This example is from 2d-07-012.

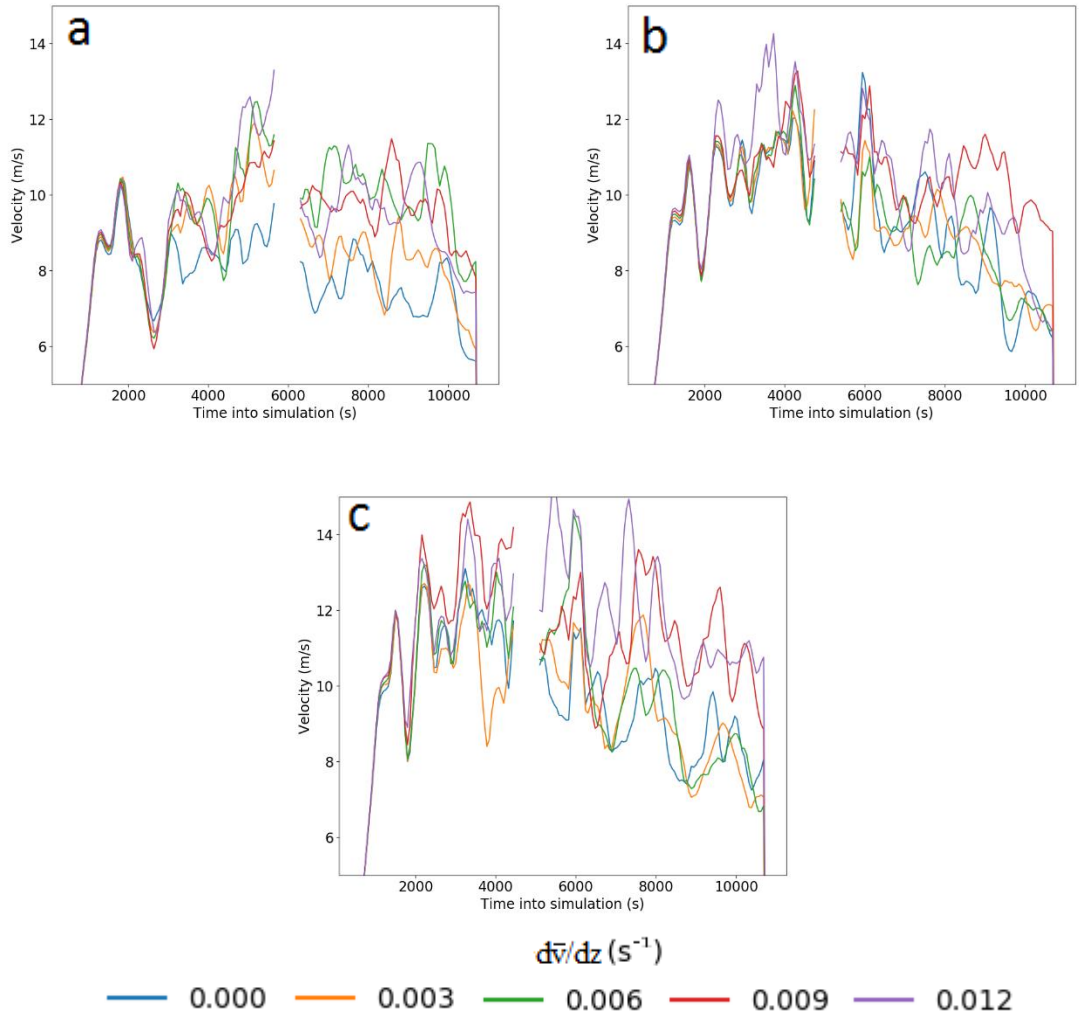

Figure 3.14: Gust front relative-*u* winds within the head the density current head time series from two dimensional simulations. Each panel represents one θ' a.) 7.0 K b.) 8.0 K c.) 9.0 K.

As the KH billows form, their centers are producing substantial negative pressure perturbations, the greatest in magnitude relative to the perturbation pressure throughout the rest of the domain. Therefore, the pressure perturbation is used as a proxy for quantifying KH billow intensity. The time series of pressure perturbation from the θ' = 7.0 K, 8.0 K, and 9.0 K simulations reveal that the higher shear environments are producing KH billows with stronger pressure perturbations, compared to their lower shear counterparts (Figure 3.15). Differences in perturbation pressure vary between 0.50 hPa and 0.75 hPa. The student *t*-test analysis also depicts this sequence (Table 3.4d,e,f). This aligns physically with the result of the gust-front relative-*u* winds. The stronger billows in the higher shear environments are associated with a stronger PGF within the density current beneath the gyre. The stronger PGF increases the strength of the surrounding flow field and is the cause of the stronger gust-front relative winds below the gyre into the head of the density currents in the high boundary-parallel vertical wind shear environments (Figure 3.16). Ultimately, this adds momentum in the positive *u* direction and sends more negatively buoyant air into the density current head. The increase in propagation speed then results in subsequent increased forced ascent, and increased CI potential.

The mixing and KH billow development are the two processes sensitive to the boundary-parallel vertical wind shear that control the propagation speed of the outflow boundaries in our simulations. The initial θ' dictates which process will dominate. In the simulations with a smaller θ' cold block and lower static stability, greater mixing due to the increased shear brings warm ambient environment air into the density current head. This reduces the negative buoyancy, and thus reduces the propagation speed. The

mechanical mixing is less in the lower boundary-parallel vertical wind shear environments. Therefore, the negative buoyancy is not greatly reduced, and thus propagates at a greater velocity. For the simulations with the larger initial θ' cold blocks, the high static stability makes the outflow boundary less susceptible to impacts from increased mechanical mixing. Thus, this does not act to reduce buoyancy as it does in the smaller θ' simulations. Rather, the increased shear within the flow provides more energy to produce stronger KH gyres with stronger pressure perturbations. As the gyres reach the ground on the backside of the density current head, a stronger pressure gradient develops that promotes a stronger cyclostrophic circulation and subsequent gust-front relative *u* wind. This adds positive momentum in the x direction to the outflow boundary, as well as advects and circulates colder, negatively buoyant air into the head. These result in an increased propagation speed of the outflow boundary in the higher shear environment.

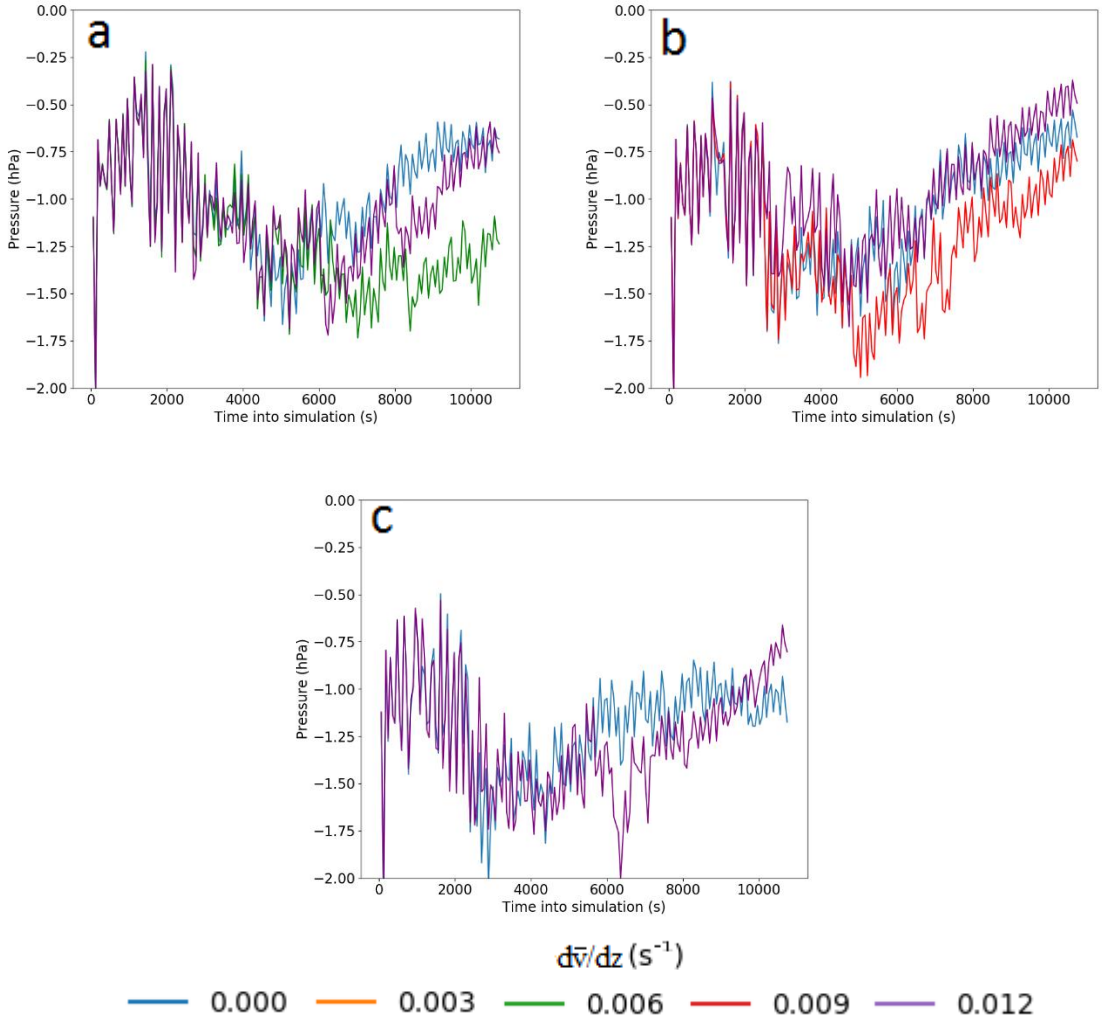

Figure 3.15: Minimum pressure perturbation time series from two dimensional simulations. Each panel represents one initial θ' a.) 7.0 K b.) 8.0 K c.) 9.0 K.

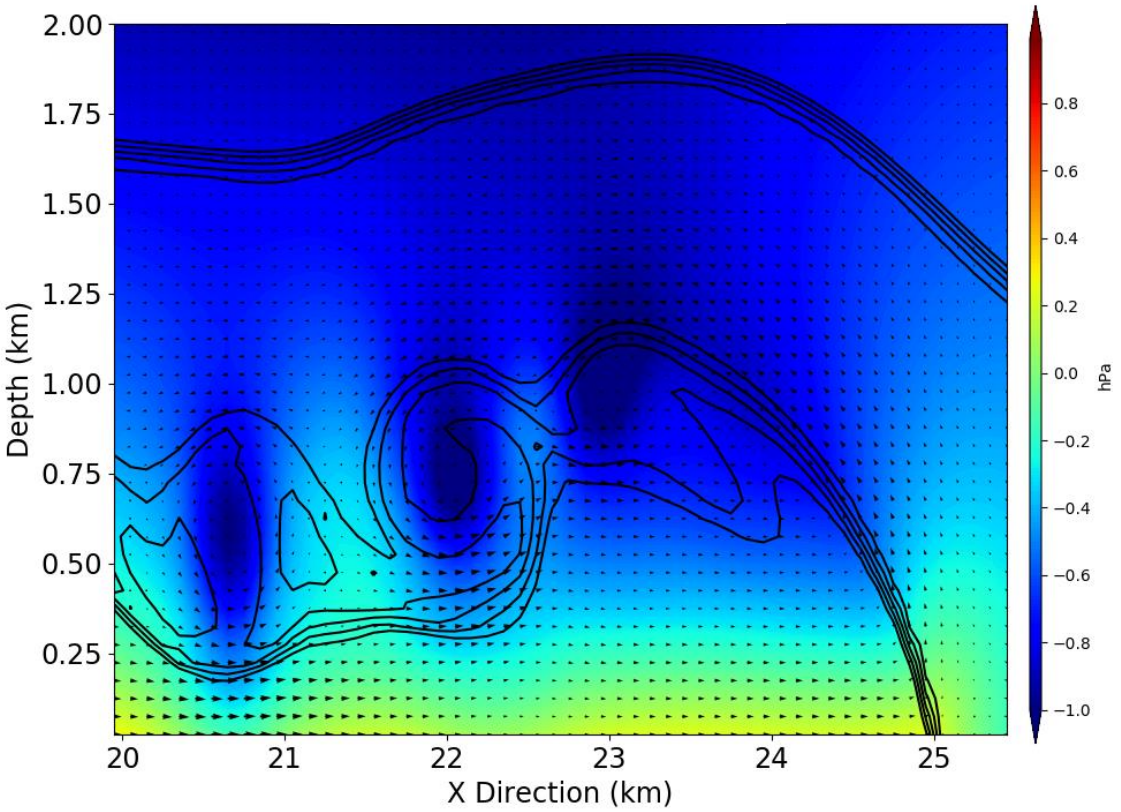

Figure 3.16: Pressure perturbations and the flow field surrounding the KH billows in the simulations. The color fill is the pressure perturbation value. The vectors represent the flow for both the *u* and *w* component of the wind. The line contours are tracer concentration used to depict the KH billows. Example is from 2d-05-000 at 6061 s.

4. Conclusion

Despite advances in instruments, convection allowing models (CAMs), and forecasting techniques, there are still many unknown factors that govern CI. Understanding of both thermodynamics and gust-front dynamics are crucial to delving into CI processes. Past studies have revealed that vertical wind shear is important in controlling attributes such as updraft erectness, density current depth, propagation speed, and convergence. However, these studies primarily focus on the boundary-normal component of the vertical wind shear vector.

Our study explores the impacts of altering the boundary-parallel component of the vertical wind shear vector, assessing changes to airmass boundary characteristics and CI potential. Thirty-five, two-dimensional simulations are conducted in CM1, testing five profiles of differing boundary-parallel vertical wind shear and seven differing air mass boundary temperatures. The differences between boundary-parallel vertical wind shear environments are examined in the fields of vertical velocity, passive-fluid tracer transport, propagation speed, and density current head depth. The depth of vertical velocity (ascent depth) and passive-fluid tracer transport are used as proxy for CI potential.

Our simulations reveal boundary characteristics and CI potential are sensitive to changes in the boundary-parallel component of the vertical wind shear. The impacts of low vs. high boundary-parallel vertical wind shear have a dependency on the initial θ' of the airmass boundary, likely related to the static stability. The boundary-parallel vertical wind shear contributes to two processes that either weaken or strengthen the airmass boundary.

The first process is the advection of warm, ambient environment air into the head of the density current induced by the mechanical mixing of the shear. The higher boundary-parallel vertical wind shear environments promote greater mechanical mixing. As warm air is transported into the head, the negative buoyancy is reduced. The reduction of negative buoyancy decreases the horizontal pressure gradient force between the boundary and environment, thus the propagation speed is slower. Ultimately, the lower propagation speed results in less forced ascent along the leading edge of the boundary and thus lower CI potential. This process of the boundary-parallel vertical wind shear controlling the mechanical mixing and advection of warm air into the head is prevalent in the simulations with the small initial θ' cold blocks. This is attributed to the weaker static stability; the small θ' boundaries are more susceptible to changes in buoyancy due to mixing. When the initial cold block has a smaller initial θ', the low boundary-parallel vertical wind shear environments are more conducive to CI than high boundary-parallel vertical wind shear environments.

In the simulations with a larger initial cold block θ', the higher shear environments have a greater amount of negative buoyancy. Therefore, the process of warm air advection into the head of the density current is not occurring. This is attributed to the increased static stability of the larger θ' boundary, making it less susceptible to impacts from warm air ingestion. Rather, the boundary-parallel vertical wind shear is affecting the strength of the KH billows that develop along the boundary interface with the ambient environment. The higher boundary-parallel vertical wind shear environments develop stronger negative pressure perturbations within the KH billow centers. As the KH gyres reach the bottom of the model domain on the back side of the density current

head, a strong pressure perturbation gradient develops. This results in positive gust-front relative *u* acceleration into the head of the density current. This increases the propagation speed by adding momentum to the density current, and also by increasing the amount of negative buoyancy as cold air from the wake of the airmass boundary is supplied to the head. The increases in propagation speed subsequently lead to increased forced ascent, and higher CI potential. Thus, in the simulations with a larger initial θ', the higher boundary-parallel vertical wind shear environments are more conducive to CI potential than the lower boundary-parallel vertical wind shear environments.

The two-dimensional simulations reveal basic impacts to boundary evolution and CI potential associated with changes to the boundary-parallel vertical wind shear. Future work will include a comprehensive analysis of three-dimensional simulations. This will have to analyze fine-scale features such as miso-vortices and individual updrafts along the leading edge of a boundary with wave-like structure. Additional three-dimensional simulations will have to be conducted that include moisture and full-physics parameterizations. Such simulations could reveal CI occurrence or CI failure. These idealized simulations will be able to provide a basic framework for future field campaigns operating unmanned aircraft vehicles (UAVs) for targeted observations along boundaries in convective environments.

References

Arnott, N.R., Y.P. Richardson, J.M. Wurman, and E.M. Rasmussen, 2006: Relationship between a weakening cold front, misocyclones, and cloud development on 10 June 2002 during IHOP. *Mon. Wea. Rev.,* **134**, 311–335, doi:10.1175/MWR3065.1.

Bryan, G. H., and J. M. Fritsch, 2002: A benchmark simulation for moist nonhydrostatic numerical models. *Mon. Wea. Rev.,* **130,** 2917-2928.

Bryan, G. H., J. C. Wyngaard, and J. M. Fritsch, 2003: Resolution requirements for the simulation of deep moist convection. *Mon. Wea. Rev.*, **131,** 2394-2416.

Buban, M.S., C.L. Ziegler, E.R. Mansell, and Y.P. Richardson, 2012: Simulation of dryline misovortex dynamics and cumulus formation. *Mon. Wea. Rev.,* **140**, 3525–3551, doi: 10.1175/MWR-D-11-00189.1.

Buban, M.S. and C.L. Ziegler, 2016: The formation of small-scale atmospheric vortices via baroclinic horizontal shearing instability. *J. Atmos. Sci.,* **73**, 2085–2104,doi: 10.1175/JAS-D-14-0385.1.

Crook, N.A., 1991: Small-scale moisture variability in the convective boundary layer and its implications for nowcasting. Preprints, *25th Int. Conf. on Radar Meteor.,* Paris, Amer. Meteor. Soc., 67-70.

Dawe, J. T. and Austin, P. H., 2012: Statistical analysis of an LES shallow cumulus cloud ensemble using a cloud tracking algorithm, *Atmos. Chem. Phys*., **12**, 1101-1119, doi:10.5194/acp-12-1101-2012, 2012.

Doswell, C.A. III, 1986. Short-range forecasting. *Mesoscale Meteorology and Forecasting.* P.S. Ray, Ed., Amer. Meteor. Soc., 689-719

Droegemeier, K.K. and R.B. Wilhelmson, 1985: Three-dimensional numerical modeling of convection produced by interacting thunderstorm outflows. part II: Variations in Vertical Wind Shear. *J. Atmos. Sci.,* **42**, 2404–2414.

Houston, A.L. and D. Niyogi, 2007: The sensitivity of convective initiation to the lapse rate of the active cloud-bearing layer. *Mon. Wea. Rev.,* **135**, 3013–3032, doi: 10.1175/MWR3449.1

Houston, A. L., 2016: The sensitivity of deep ascent of cold-pool air to vertical shear and cold-pool buoyancy. *Electronic J. Severe Storms Meteor*., **11** (3), 1–29.

Lee, B.D. and R.B. Wilhelmson, 1997: The numerical simulation of non-supercell tornadogenesis. Part I: Initiation and evolution of pretornadic misocyclone circulations along a dry outflow boundary. *J. Atmos. Sci.,* **54**, 32–60, doi: 10.1175/1520-0469(1997)054<0032:TNSONS>2.0.CO;2.

Lee, B.D. and R.B. Wilhelmson, 1997: The numerical simulation of nonsupercell tornadogenesis. Part II: Evolution of a family of tornadoes along a weak outflow boundary. *J. Atmos. Sci.,* **54**, 2387–2415, doi: 10.1175/1520-0469(1997)054<2387:TNSONT>2.0.CO;2.

Madaus, L.E. and G.J. Hakim, 2016: Observable surface anomalies preceding simulated isolated convective initiation. *Mon. Wea. Rev.,* **144**, 2265–2284, doi: 10.1175/MWR-D-15-0332.1.

Marquis, J.N., Y.P. Richardson, and J.M. Wurman, 2007: Kinematic observations of misocyclones along boundaries during IHOP. *Mon. Wea. Rev.,* **135**, 1749–1768, doi: 10.1175/MWR3367.1.

Mellado, J.P., B. Stevens, and H. Schmidt, 2014: Wind shear and buoyancy reversal at the top of stratocumulus. *J. Atmos. Sci.,* **71**, 1040–1057,https://doi.org/10.1175/JAS-D-13-0189.1

Moncrieff, M.W. and C. Liu, 1999: Convection initiation by density currents: Role of convergence, shear, and dynamical organization. *Mon. Wea. Rev.,* **127**, 2455–2464, doi: 10.1175/1520-0493(1999)127<2455:CIBDCR>2.0.CO;2.

Murphey, H. V., R. M. Wakimoto, C. Flamant, and D. E. Kingsmill, 2006: Dryline on 19 June 2002 during IHOP. Part I: Airborne doppler and LEANDRE II analysis of the thin line structure and convection initiation. *Mon. Wea. Rev.*, **134,** 406–430.

Neggers, R.A., A.P. Siebesma, and H.J. Jonker, 2002: A multiparcel model for shallow cumulus convection. *J. Atmos. Sci.,* **59**, 1655–1668, https://doi.org/10.1175/1520-0469(2002)059<1655:AMMFSC>2.0.CO;2

Roebber, P.J., D.M. Schultz, B.A. Colle, and D.J. Stensrud, 2004: Toward improved prediction: High-resolution and ensemble modeling systems in operations. *Wea. Forecasting*, **19**, 936–949, https://doi.org/10.1175/1520-0434(2004)019<0936:TIPHAE>2.0.CO;2

Romps, D.M. and Z. Kuang, 2010: Nature versus nurture in shallow convection. *J. Atmos. Sci.,* **67**, 1655–1666, doi: 10.1175/2009JAS3307.1.

Rousseau-Rizzi, R., D.J. Kirshbaum, and M. Yau, 2017: Initiation of deep convection over an idealized mesoscale convergence line. *J. Atmos. Sci.,* **74**, 835–853, doi: 10.1175/JAS-D-16-0221.1.

Schumacher, R.S., 2015: Resolution dependence of initiation and upscale growth of deep convection in convection-allowing forecasts of the 31 May–1 June 2013 supercell and MCS. *Mon. Wea. Rev.*, **143**, 4331–4354, doi: 10.1175/MWR-D-15-0179.1.

von Karman, T., 1940: The engineer grapples with nonlinear problems. *Bull. Amer. Math. Soc.* **46**, 615-683.

Weckwerth, T.M. and D.B. Parsons, 2006: A review of convection initiation and motivation for IHOP 2002. *Mon. Wea. Rev.,* **134**, 5–22, doi: 10.1175/MWR3067.1.

Wilson, J.W., G. Foote, N. Crook, J.C. Fankhauser, C.G. Wade, J.D. Tuttle, C.K. Mueller, and S.K. Krueger, 1992: The role of boundary-layer convergence zones and horizontal rolls in the initiation of thunderstorms: A case study. *Mon. Wea. Rev.*, **120**, 1785–1815, doi: 10.1175/1520-0493(1992)120<1785:TROBLC>2.0.CO;2.

Wilson, J.W. and R.D. Roberts, 2006: Summary of convective storm initiation and evolution during IHOP: Observational and modeling perspective. *Mon. Wea. Rev.*,**134**, 23–47, doi: 10.1175/MWR3069.1.

Wu, X. and M. Yanai, 1994: Effects of vertical wind shear on the cumulus transport of momentum: Observations and parameterization. *J. Atmos. Sci.*, **51**, 1640–1660,https://doi.org/10.1175/1520-0469(1994)051<1640:EOVWSO>2.0.CO;2

Xu, Q., 1992: Density currents in shear flows-a two-fluid model. *J. Atmos. Sci.*, **49**, 511–524, doi: 10.1175/1520-0469(1992)049<0511:DCISFA>2.0.CO;2.

Xu, Q., M. Xue, and K.K. Droegemeer, 1996: Numerical simulations of density currents in sheared environments within a vertically confined channel. *J. Atmos. Sci.*, **53**,770–786, https://doi.org/10.1175/1520-0469(1996)053<0770:NSODCI>2.0.CO;2

Ziegler, C.L. and E.N. Rasmussen, 1998: The initiation of moist convection at the dryline: Forecasting issues from a case study perspective. *Wea. Forecasting*, **13**,1106–1131, doi: 10.1175/1520-0434(1998)013<1106:TIOMCA>2.0.CO;2.

Ziegler, C. L., E. N. Rasmussen, M. S. Buban, Y. P. Richardson, L. J. Miller, and R. M. Rabin, 2007: The “Triple point” on 24 May 2002 during IHOP. Part II: Ground-radar and in situ boundary layer analysis of cumulus development and convection Initiation. *Mon. Wea. Rev.*, **135,** 2443–2472.